ASSOCIATION EURATOM - UNIVERSITY OF LATVIA

AEUL

ANNUAL REPORT 2013

Riga 2014

TABLE OF CONTENT

1. INTRODUCTION

This Annual Report summarizes the fusion research activities of the Latvian Research Unit of the Association EURATOM-University of Latvia (AEUL) in 2013.

Association EURATOM – University of Latvia has been playing an active part in previous consultations on the future structure of the EURATOM programme. Since the EC decided that the Contract of Associations should be replaced by Consortium Agreement, the AEUL anticipate a similar multiannual contract with Latvian Fusion Laboratory under party *University of Latvia, Institute of Solid State Physics*, saving groups of our fusion *professionals* and *technicians* on base of specialisation continuity.

Alongside with this we hope that a new structure will ensure equivalence for all participants in particular for Fusion Laboratories in smaller Member States.

Recently we have signed the Memorandum of Understanding and the Consortium Agreement, and prepared the documentation for the Grant Agreement.

The Physics Programme is carried out at IP UL – Institute of Physics, University of Latvia, and at ISSP UL – Institute of Solid State Physics, University of Latvia.

The research areas of the Physics Programme are:

- Stability of metal droplets jets in tokamak environment ;

Theory and Code Development:

- Analysis of equations arising in gyrotron theory;
- Regions of azimuthal instability in gyrotrons;
- Analysis of aftercavity interaction in European ITER gyrotrons and in the compact sub-THz gyrotron FU CW-CI;
- Ab initio simulations of the reduced activation steels strengthened by yttria precipitates;

The Technology Programme is carried at ICP UL - Institute of Chemical Physics, University of Latvia. The technology research and development under EFDA JET is focused on:

- Analysis of accumulated tritium and microstructure of carbon based jet divertor tiles;
- Tritium release from high dose neutron irradiated HIDOBE-01 beryllium pebbles;
- Influence of chemisorption products on radiolysis of lithium orthosilicate.

Finally I wish to thank all the staff members of AEUL for their contribution and Latvian Ministry of Education and Sciences for continuous support.

Riga, August 2014

(Andris Sternberg, Head of Research Unit of AEUL)

2. FUSION PROGRAMME ORGANISTION

2.1 Programme Objectives

The Latvian Fusion Programme, under the Association EURATOM-University of Latvia, is fully integrated into the European Programme, which has set the long-term aim of the joint creation of prototype reactors for power stations to meet the needs of society: operational safety, environmental compatibility and economic viability. The objectives of the Latvian programme are: (i) to carry out high-level scientific and technological research in the field of nuclear fusion, (ii) to make a valuable and visible contribution to the European Fusion Programme and to the international ITER Project in our focus areas. This can be achieved by close collaboration with other Associations.

2.2 Association EURATOM-University of Latvia (AEUL)

The Latvian contribution to the European fusion programme began in 2000 in the form of cost-sharing actions (fixed contribution contracts with EURATOM). The Association was established on 19 December 2001 incorporating the existing cost-sharing actions into its work plan.

2.3 Fusion Research Units

The Latvian Research Unit of the Association EURATOM-University of Latvia consists of three Institutes of University of Latvia.

1. IP UL – Institute of Physics, University of Latvia
   32 Miera St., Salaspils LV-2169, Latvia.
   Phone +371 6 7944700, Fax. +371 6 7901214
2. ISSP UL – Institute of Solid State Physics, University of Latvia
   8 Kengaraga St., Riga LV-1063, Latvia.
   Phone +371 6 7187810, Fax. +371 6 7132778
3. ICP UL - Institute of Chemical Physics, University of Latvia
   4 Kronvalda Blvd., Riga LV-1010, Latvia.
   Phone +371 6 7033884, Fax. +371 6 7033884

2.4 Association Steering Committee

The research activities of the Latvian Association EURATOM-University of Latvia are directed by the Steering Committee, which comprises the following members in 2012:

Mr. Vito Marchese Scientific Officer, Unit RTD - K6

Mr. Rugero Giannella Scientific Officer, Unit RTD - K6

Mr. M. Cosyns, Administration and finance, Unit RTD – K7

Mrs. Irina Arhipova, Ministry of Education and Science

Mr. Ivars Lacis, University of Latvia

Mr. Andrejs Silins, Latvian Academy of Sciences

The Steering Committee had one meeting in 2013. This meeting was organised on July 2, 2013 with remote participation of EU Commission representatives.

2.5 The Latvian Members in the EU Fusion Committees

Consultative Committee for the EURATOM Specific Research and Training Programme in the Field of Nuclear Energy-Fusion (CCE-FU)

Mr. Andris Sternberg, ISSP UL

EFDA Steering Committee

Mr. Andris Sternberg, ISSP UL

Governing Board for the Joint European Undertaking for ITER and the Development of Fusion Energy, "Fusion for Energy" (F4E GB)

Mrs. Maija Bundule, Latvian Academy of Sciences

Mr. Andris Sternberg, ISSP UL

EFDA Public Information Group(recently – Public Information Network – PIN)

Mr. Maris Kundzins, ISSP UL

2.6 Public Information

Conferences

Results of fusion research were presented at:

- The annual scientific conference of University of Latvia.

- The 28th and 29th Scientific Conferences of Institute of Solid State Physics, University of Latvia.
- International Conferences "Functional Materials and Nanotechnologies" (FM&NT-2012) Riga, Institute of Solid State Physics, University of Latvia
- FM&NT-2013, Institute of Physics, Tartu University, Estonia.

Educational activities

Excursions at ISSP UL from schools were organized two to three times a month for PhD students from Latvian universities. Booklets about ISSP UL and EFDA were distributed.

Television, press

Presentation in the television broadcasts TV1, TV7, TV24 and interviews in the newspapers "Diena" and "Dienas Bizness".
 Presentations in Radio – popular science broadcast.

Popularization of science

Presentation in the TV programme "Science in Latvia",
Presentation in the programme "Researchers Night in Latvia" on 26th of September, 2013

3. PHYSICS PROGRAMME – FUSION PHYSICS

EFDA-Power Plant Physics & Technology

Task Agreement WP13-PEX-03b-T05-01/University of Latvia/BS

Task Area: Novel PFC material solutions - Liquid Metals
TA Title: First simulations concerning liquid metals in tokamaks divertor - CPS and free flowing liquids .
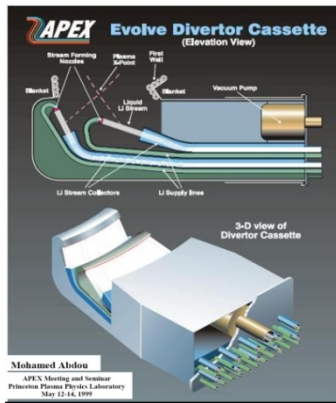

Principal investigator: E. Platacis.
Staff members: O.Lielausis, A.Klukins, I.Kaldre, J.Peinbergs.

3.1. First simulations concerning liquid metals in tokamaks divertor

Introduction
Fast liquid metal jets as plasma facing components were present already in the very first proposals when liquid metals where considered as useful for divertor protection and , in the same time, for the extraction of the power . A high power load capability should be considered as the most distinctive and attractive feature of these proposals, especially, if materials like Ga or Sn are accepted and high velocities (v>5m/s) allowed. Estimates show that loads of the order of 50 MW/m^2 and even higher could be expected. Already in 1986 on the small tokomak T-3M an essential result was achieved, namely, it was shown that after a contact with a high-Z liquid metal the plasma can remain alive[1]. The plasma touched upon a screen of InGaSn droplets, however, the discharges remained practically unchanged. For the given report essential are the results gained during joint experiments on ISTTOK where the plasma was interacting directly with a Ga jet[2]. The workability of the developed Ga stand was confirmed, Ga-technology under tokamak relevant conditions mastered[3].   It was stated again that the contact of the plasma with Ga does not influence essentially the discharge. Most important is the conclusion about the ability of liquid metal jets to absorb and transfer high indeed power loads .During the 25 ms of discharge the plasma was contacting approx. 0.25 cm^3 of Ga. The temperature of this volume jumped for 103^{0}C. It means that by the jet 2.4 kW of power were extracted. Considering the power deposition as fully frontal a load of the order of 20 MW/m^2 could be deduced. The continuity of jet was fully preserved. Earlier doubts were expressed that at such high loads the LM body should "explode" because of the non-homogeneity in the power deposition, because of the presence of diffused gases etc. Finally, the old problem about the spatial stability of such free flying jets was actualized – during the discharge a definite deflection of the jet was detected.[5]

Application: LM divertors for tokamaks

Main aim: to get a stable system of jets, which are able absorb heat fluxes of up to 50 MW/m²

Liquid metal: Li, Ga

Magnetic field: ~ 5-10 T

Velocities: ~ 1 – 10 m/s

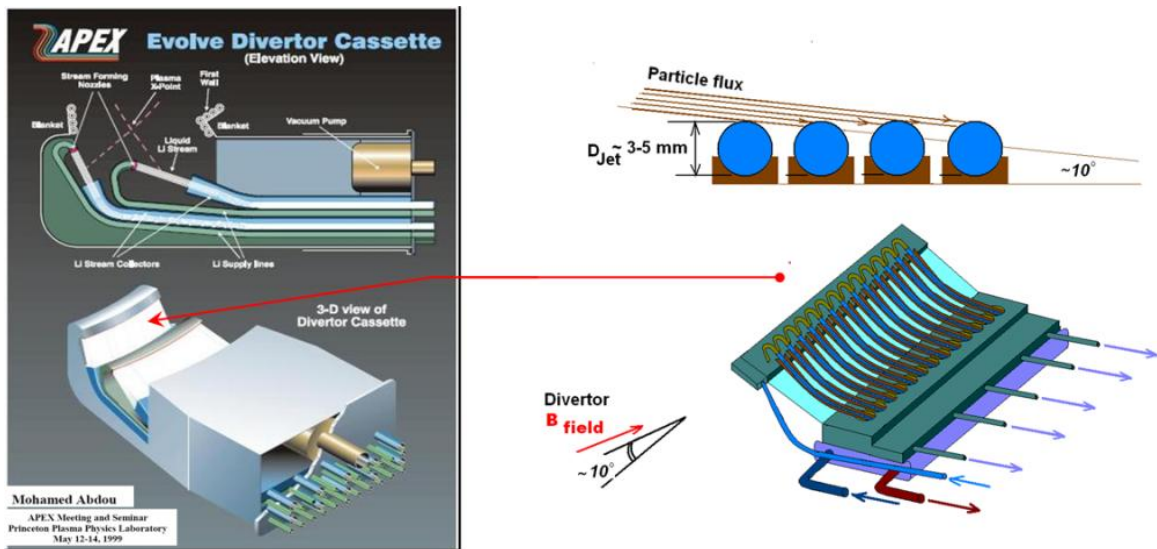Figure 3.1.1. Scheme of a free flying LM jet protected divertor [7]

Figure 3.1.2. Scheme of a divertor protected by LM jets over curved substrates.

MHD experiments on LM Jets passing over curved substrates
The results of 2013 were in a definite sense unexpected. It was stated that in the presence of a strong up to 4T field the path of a jet can be effectively controlled and guided by means of curved solid substrate or rails [6]. As a base for comparison (Fig.3.1.1)a concrete scheme of a LM jet protected divertor was chosen [7]. Also the general motivation was taken from this publication- to get a stable system of jets, which are able to absorb heat fluxes of up to 50 MW/m2. We are showing (Fig.3.1.2) that in principle the free flying jets could be replaced by jets running over curved rails. The high power load capability of the system would remain practically on the same level, however, the stability of the system would be essentially increased. Our 2013 results are indicating that there are grounds for promotion of such an idea. The main components of the experimental setup are shown in Fig.3.1.3 Our cryogen-less superconducting magnet (5T in a D=30cm; L=100cm bore) was used. In the bore a cylindrical container was placed containing containing curved guiding substrates of different kind Figures 1.4,5,6. The jets were generated by three parallel d= 2.3 mm medical needles issuing from a cylindrical Plexiglas outlet. The system was connected

9

to our InGaSn stand. The container inside the magnet together with the inlet and outlet piping can also bee seen. As most informative the Fig.4 should be considered. The three jets have been targeted towards a smooth curved (R= 95mm) SS wall. The angle of incidence was kept equal to 30^0. The wall was not especially prepared, it means, in this case the jets were targeted towards a non-wetted badly conducting substrate. The result was somewhat striking. In up to 4T fields the jets remained stable and well-organized over the full length (200mm) of their path. Even at such an rather blunt angle they clearly wanted to remain standing apart. Fig.3.1.5 represents a case when the wall is ideally wetted. Simply, the jets were targeting an especially prepared/wetted Cu insert. As expected, without the field because of the good wettability the jets tended to form a film-like cover. In the presence of a strong field the picture becomes unstable, difficult to describe. The induced forces are tending even to separate the flow from the substrate, to lift small sub-volumes, etc. It is a new example in our experience how. It is difficult it is to generate film-like motions in the presence of strong fields. We had to learn it once more. In Fig.3.1.5 again a non-prepared plate can seen, curved at R=72.5mm. The plate was installed independently, could be turned, also the angle of incidence could be changed. From the corresponding results we are representing the case when at the end /outlet of the plate a deflector was installed, turning the jets down, towards the draining opening of the chamber. Under definite conditions a stable motion over such a complex path can be organized.

In a tokamak environment a good wettability/contactability of the active surfaces should be taken into account, at least, potentially. Correspondingly, neighboring jets could also start interacting, because of the appearance of capillary and specific em forces. To avoid such disturbances we are considering versions when each jet is running along its own rail which is separated/isolated from the neighbors (Fig.3.1.6). In the first case the rails or grooves were maid of stainless steel (non-wetted, non-contacting). In the second case the rails were made of cupper with a properly prepared surface for a good wettability/contactability. In both cases the rails were perfectly conducting the path of the jets.
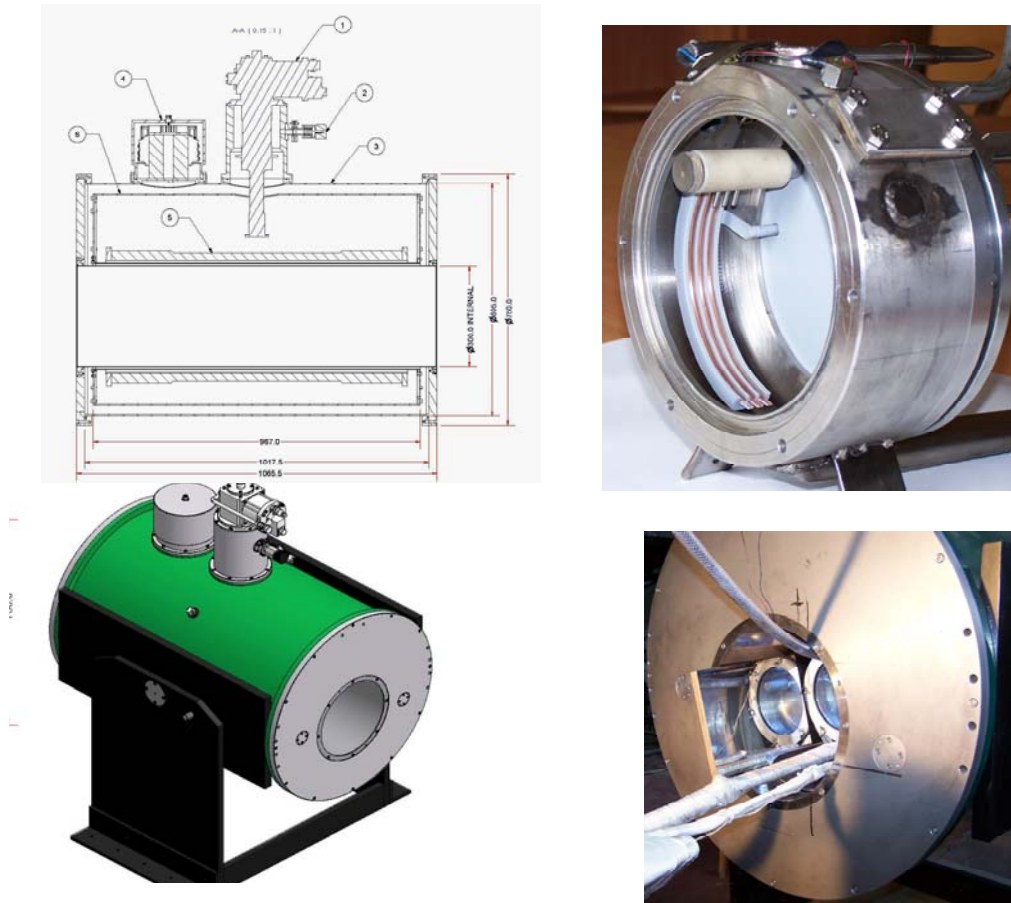
Figure 3.1.3. Main components of the experimental setup.

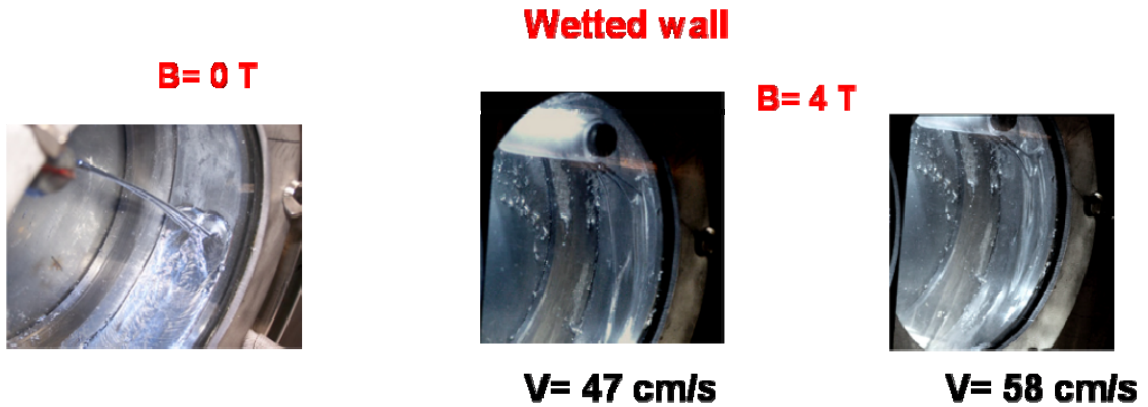Figure 3.1.4. Flow over non-wetted curved substrates.

Figure 3.1.5. Flow over wetted curved substrates.

Figure 3.1.6 Flow over non-wetted substrates with deflector.

Conclusions

1. Curved solid substrates can be successfully used for spatial fixation of fast moving liquid metal jets in the presence of strong magnetic fields, in other words, to prevent free flying liquid metal jets from deflection. At present, it is difficult to give a clear explanation of such an intriguing behavior of the jets.

2. In principle, in liquid metal protected divertors, the free flying jets could be replaced by jets flowing over the curved solid substrates. The high power extraction capability would remain practically non-affected, however, the stability of the system would be essentially enhanced.

References

[1] A.F.Kolesnichenko, E.V.Murav'ev, V.N.Dem'janenko, B.O.Karasev,I.V. Lavrent'ev, O.A.Lielausis, A.V.Tananaev, "Research and development liquid metal system for a tokamak reactor".Fusion Eng.& Design, (1989_, No.8, pp.283-288.

[2] Gomes R.B.,Fernandes H., Silva C., Sarakovskis A., Pereira T., Figueiredo J., Carvalho B., Soares A., Varandas C., Lielausis O., Klykin A., Platacis E., Tale I.: Interaction of

liquid gallium jet with the tokamak ISTTOK edge plasma. Fusion Eng. & Des., 83(2008)102-111

[3] O. Lielausis, A. Klykin, E. Platacis, A. Mikelsons, R.B. Gomes, H. Fernandes, C. Silva "Stability of liquid metal jet in the context of fusion applications" Proc. Int. Conf. Fundamental and applied MHD, Pamir 2011 V.1, p.257-260.- Borgo-Corsica-France September 5-9, 2011

[4] Gomes R.B.,Fernandes H., Silva C., Sarakovskis A., Pereira T., Figueiredo J., Carvalho B., Soares A., Duarte P., Varandas C., Lielausis O., Klykin A., Platacis E., Tale I., Alekseyev A.: Liquid gallium jet-plasma interaction studies in ISTTOK tokamak. Journ.of Nuclear Materials 390-391(2009)938-94

[5] Gomes R.B., Silva C., Fernandes H., Duarte P., Lielausis O., Klykin A., Platacis E. Dynamic behavior of a Liquid Gallium Jet under the influence of the Tokamak ISTTOK Plasmas; 19 Internat. Conf. on Plasma Surface Interaction., P2-83, May 24-28 (2010) Sam Diego, USA.

[6] O.Lielausis, A.Klukins, E.Platacis.: "MHD experiments on LM jets passing over curved substrates", "3d International Symposium on Lithium applications for Fusion Devices", ISLA2013, October 9-11, 2013,C.R.ENEA Frascati

[7] M.Abdou, Report on APEX meeting and Seminar , PPPL, May 12-14, 1999.

3.2. CPS-Modelling the convection in the porous structure.
1. **To quantify the influence of EM forces on renewal of surface by capillary forces**
2. **To identify the main parameters affecting MHD flows in CPS**

Introduction

Thermoelectric forces may have a significant role on the liquid lithium flow in the fusion reactor divertor. Lithium has particularly high absolute thermoelectric power (up to 30 μV/K). Thermoelectric current is created at the boundary between two different media, by applied temperature gradient. If magnetic field is present then electric current and field interaction creates force which may drive a liquid convection or create pressure distribution in the liquid lithium. Idea to use thermoelectric pumping effect to remove excess heat from divertor zone has been explored in last few years (D.N. Ruzic, 2010). Results have shown that these effects can be quite strong in liquid lithium subjected to high local temperature gradients. In this work authors present the idea to use thermoelectric current and magnetic field created pumping effect of liquid lithium. In such case cooling lithium flow is driven by applied field and heat flow. Newest results of their work have been reported recently in 3rd international symposium on lithium applications for fusion devices. Significant pumping velocities may be achieved.

In this chapter we estimate the order of magnitude of thermoelectric forces in several different cases in comparison with gravity, capillarity and other forces. Aim of this work is to demonstrate the significance of these forces and to raise awareness about negative effects which may emerge due to high thermoelectric properties of lithium. Macroscopic lithium flow and microflow in one capillary has been analyzed numerically and characteristic force densities have been estimated based on results. Liquid lithium/Stainless steel wool CPS subjected to inhomogeneous heat flow from plasma has been analyzed numerically. It is demonstrated that local heat pulse from plasma may cause forces which pushes lithium into plasma and away from hottest place. These forces may exceed gravity and capillarity. This phenomena needs to be deeper evaluated and understand, because

uneven heat flow and tangential temperature gradient on the CPS/plasma boundary is present.

Thermoelectric magnetohydrodynamics

The term thermoelelectric magnetohydrodynamics was introduced by Shercliff (Shercliff J. , 1979) in the seventies of 20th century. He developed the idea that thermoelectric current in the presence of magnetic field can cause stirring or pumping of liquid conducting media. He also presented the order of magnitude estimation for a practical magnitude of TEMC velocity, showing that velocity which can be reached in the liquid lithium under high temperature gradient which can be reached in fusion reactors (*grad(T)*≈10 K/mm, *B*=1 T, S_{Li}=25 µV/K) can reach up to 25 cm/s. This principle was exploited by developing thermoelectric pumps, which were also used in practice for cooling of space ships nuclear reactors. In these pumps flow is driven by the temperature difference between the heater and cooler. If heat source is reactor itself, then positive feedback exists and the higher is reactor temperature, the higher is flow velocity in cooling circuit and cooling is more effective (Polzin, 2007).

Relation describing the electric current flow in the continuous media is Ohm's law. Thus electric current in the media can be also caused by temperature gradient; law can be generalized by including thermoelectric term.

$$\frac{\vec{j}}{\sigma} = \vec{E} + \vec{u} \times \vec{B} - S\nabla T$$

TEMC in the liquid phase has been created by thermoelectric current, driven by Seebeck voltage at the contact surface between two different materials, and applied magnetic field interaction causing Lorentz force

$$\vec{F} = \vec{j} \times \vec{B}$$

Thermoelectric current in liquid media can be expressed from Ohm's law. Melt motion is described by Navier-Stokes equation:

$$\rho\left(\frac{\partial \vec{u}}{\partial t} + \vec{u} \cdot \nabla \vec{u}\right) = -\nabla p + \mu\nabla^2\vec{u} + \vec{j} \times \vec{B}$$

From these two equations we get the following equation:

$$\rho\left(\frac{\partial \vec{u}}{\partial t} + \vec{u} \cdot \nabla \vec{u}\right) = -\nabla p + \mu\nabla^2\vec{u} + \sigma\left(\vec{u} \times \vec{B} \times \vec{B} - S\nabla T \times \vec{B}\right)$$

Applied magnetic field introduces two new terms in the Navier-Stokes equation. Term $\sigma S\nabla T \times \vec{B}$ is thermoelectric term, which creates thermoelectromagnetic convection in the melt. Whereas term $\sigma\vec{u} \times \vec{B} \times \vec{B}$ is magnetohydrodynamic braking force which is created by the conducting fluid motion in magnetic field, this force always acts opposite to the fluid velocity. As we see, thermoelectric force is proportional to magnetic field while MHD braking force is proportional to *B* square. This means that at low magnetic field values thermoelectric force is dominant, but as *B* increases, eventually braking force grows faster and finally exceeds thermoelectric force and further increase of magnetic field reduces the convection intensity. This effect has been exploited to damp unwanted natural convection (Davoust, Bertrand, Moreau, Tanguy, & Bolcato, 1997). From here, an important conclusion can be made: Thermoelectromagnetic convection intensity has a maximum at certain magnetic field value when thermoelectric and braking forces are in balance. First publications on the effect of liquid phase motion in static field appeared in the second half of twentieth century when semiconductor production became an actual problem. This problem has been investigated by Institute of Physics University of Latvia (Gorbunov L. ,

14

1987). The idea of influencing the interdendritic convection by magnetic field during solidification is relatively new and was introduced by Moreau and Lehmann (Lehmann, Camel, & Bolcato, 1998) in the nineties. Temperature gradient at the solidification front can be quite high thus even with moderate magnetic field quite strong convection can be reached. Solute and energy transport due to this convection may then affect macrosegregation, cell and dendrite morphology and even solidification front shape.

Simplified Navier-Stokes can be solved to estimate the TEMC velocity as a function of magnetic field. In case of a flow we may expect similar trend also for different materials. At large length scales and high magnetic fields TE flow of conducting media is limited by MHD braking force while at smaller length scales velocity maximum is reached at higher field values as demonstrated in Figure 3.2.1.

$$\rho \frac{u^2}{L} + \mu \frac{u}{L^2} + c\sigma \ (uB^2 - P\theta B) = 0$$
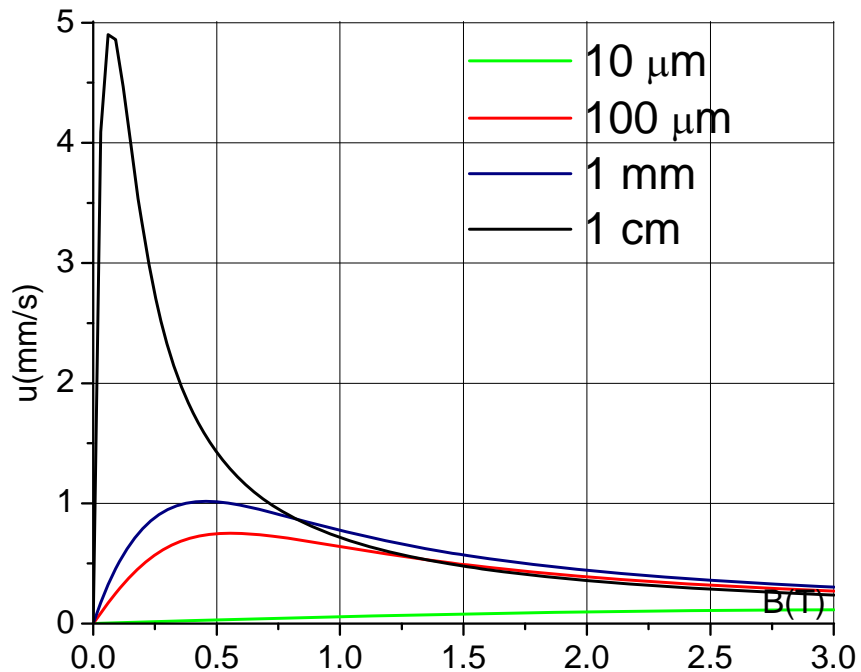
Figure 3.2.1. TEMC velocity order of magnitude at four different length scales (properties of Sn-wt.10%.Pb are used, θ=8 K/mm)

Analysis of macroscopic TE effects along CPS/SS interface

Porous media is 2/3 ss and 1/3 Li by volume. Porous media was modeled as wire mesh packet. Overall scheme is shown in Figure 3.2.2.
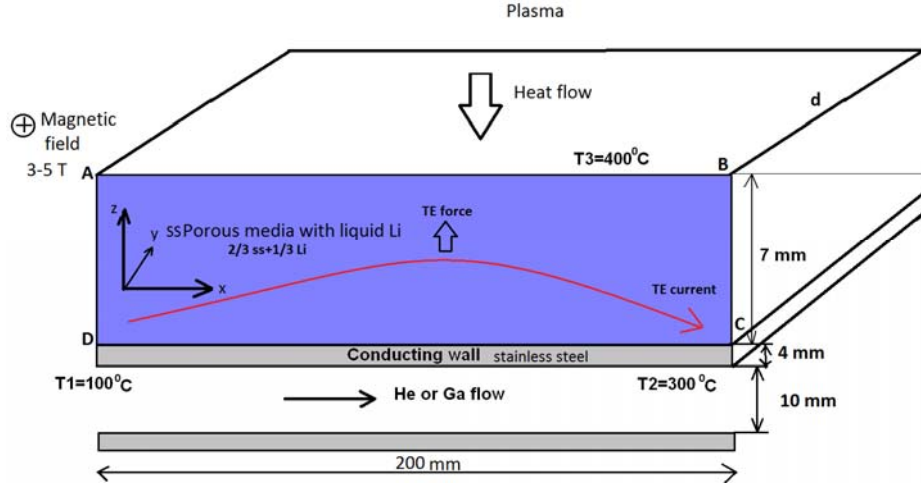
Figure 3.2.2: Schematics of numerical model and boundary conditions. 7mm thick CPS layer is separated from Gallium flow with 4 mm SS wall

Table 1: Physical properties of materials ((GaInSn properties, 1982), (Wang, et al., 2012))

Property	Symbol	Lithium	Stainless steel	Porous media	Gallium	Unit
Thermal conductivity	λ	44	16	26	35	W/m*K
Heat capacity	C	4350	500	1800	400	J/kg*K
Electrical conductivity	σ	$3.6 \cdot 10^6$	$1.3 \cdot 10^6$	$2 \cdot 10^6$	$3.6 \cdot 10^6$	Sim/m
Absolute thermoelectric power	S	20	0	7	0	μV/K
Density	ρ	500	7500	5000	6000	Kg/m^3
Surface tension	γ	0.32				N/m
Viscosity	μ	$6 \cdot 10^{-4}$			0.0021	Pa*s

Boundary conditions: Boundary between CPS and steel generates thermoelectric voltage φ=T·ΔS.

Electric current order of magnitude can be estimated as

$$j = \sigma\theta\Delta S = 1.4 \cdot 10^4 \, A/m^2$$

Thermoelectric current interacts with magnetic field and Lorentz force is generated.

$$\vec{F} = \vec{j} \times \vec{B} = \begin{pmatrix} j_x & j_y & j_z \\ 0 & B & 0 \\ \vec{i} & \vec{j} & \vec{k} \end{pmatrix} = j_x B\vec{k} - j_z B\vec{i}$$

In the liquid region: Ohm's law:

$$\vec{j_l} = -\sigma_l \vec{\nabla} V_l - \sigma_l S_l G \vec{i}_y,$$

where σ_l and S_l respectively denote the electrical conductivity and the thermo-electric constant of the liquid

Continuity: $\vec{\nabla}.\vec{j} = 0$ so that $\nabla^2 V_l = 0$ and V_l is harmonic in the solid region:

Same equations as before:

$$\vec{j}_s = -\sigma_s \vec{\nabla} V_s - \sigma_s S_s G \vec{i}_y \text{ and } \nabla^2 V_s = 0 \ ;$$

Boundary condition at the liq.-sol. interface

- Continuity of the normal component of the electric current:

$$-\sigma_l \frac{\partial V_l}{\partial n} - \sigma_l S_l G \vec{i}_y.\vec{n} = -\sigma_s \frac{\partial V_s}{\partial n} - \sigma_s S_s G \vec{i}_y.\vec{n} \ ,$$

- Continuity of the scalar potential: $V_s = V_l$.

Boundary conditions at the external boundary everywhere on the outer boundary $\dfrac{\partial V_l}{\partial n} = 0$

. In case of 2D current flow force field is curl-free, thus pressure field is created but no liquid flow is induced [3]. Tetrahedral mesh consisting of 40460 elements. Calculated current and force is shown in Figure 3.2.3.
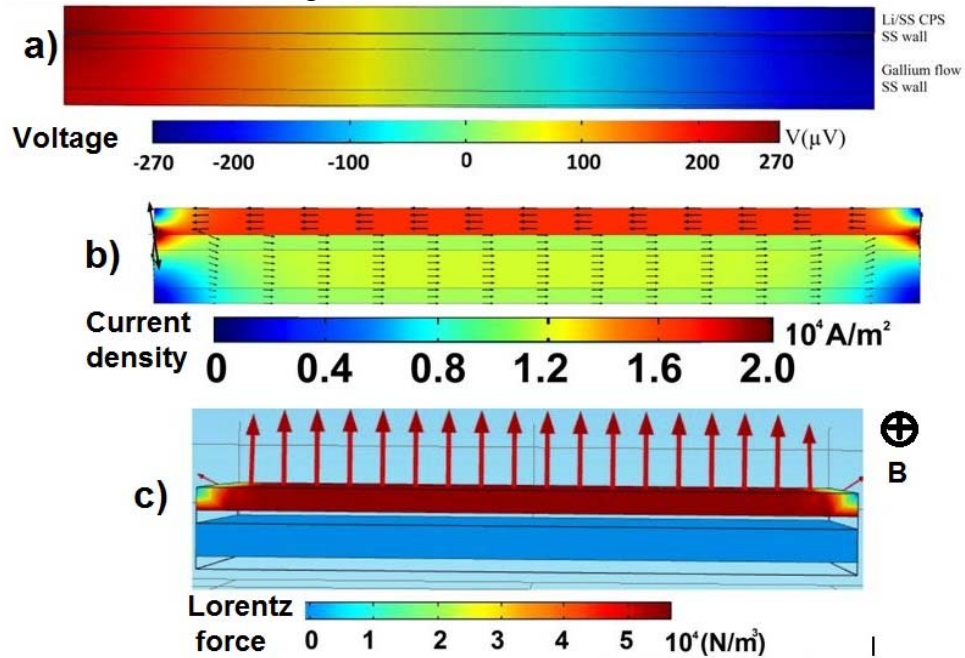

Figure 3.2.3: a) Thermoelectric voltage. b) Thermoelectric current density. c) Lorentz force density in CPS.

Analysis of microflow inside one separate capillary

CPS consists of array of 0.5 mm diameter capillaries with 0.1 mm thick SS walls. Li evaporates from boundary between CPS and plasma as can be seen from Figure 3.2.4.
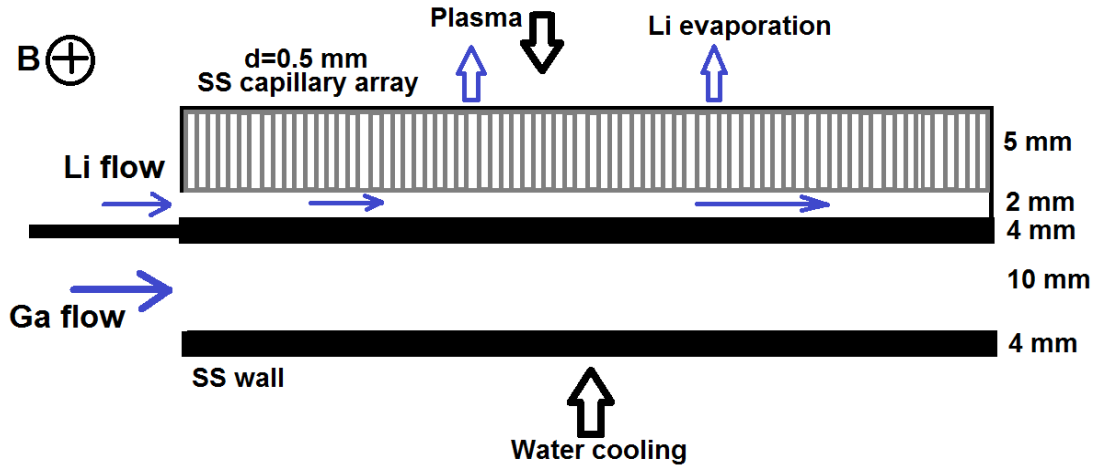
Figure 3.2.4: Experimental scheme (xz plane). CPS consists of array of 0.5 mm SS capillaries delivering liquid Li to the surface

Numerical model: L=5 mm long capillary is numerically simulated. Temperature difference between the ends of the capillary is 200 K, inner diameter d=0.5 mm, wall thickness 0.1 mm, Li flow in the capillary is v=2 m/s to ensure sufficient amount of Li on the surface of CPS/Plasma.

Forces acting on liquid Lithium and their magnitude estimations:

- Capillary force

$$F_c = 4\frac{\gamma}{dL}$$ (55 N/cm³)

- Gravity force

$$F_g = \rho g$$ (0.5 N/cm³)

- Thermoelectromagnetic force

in capillary $F_{TE} = \dfrac{\sigma \Delta S \theta B}{5}$ (100 N/cm³)

macroscale TEMC-see figure 5 (5 N/cm³)

- Electromagnetic force

$$F_e = \sigma u B^2$$ (3000 N/cm³)

- Viscous force (Poiseuille flow)

$$F_v = \frac{32\mu v}{d^2}$$ (15 N/cm³)

Order of magnitude estimations of forces shows that main force affecting flow is electromagnetic force due to rapid liquid motion perpendicular to strong magnetic field. Thermoelectric force and capillary forces are second most important forces according to this estimation. Figure 3.2.5 confirms this estimation. It can be seen that Lorentz force is homogeneous in the volume of the capillary.
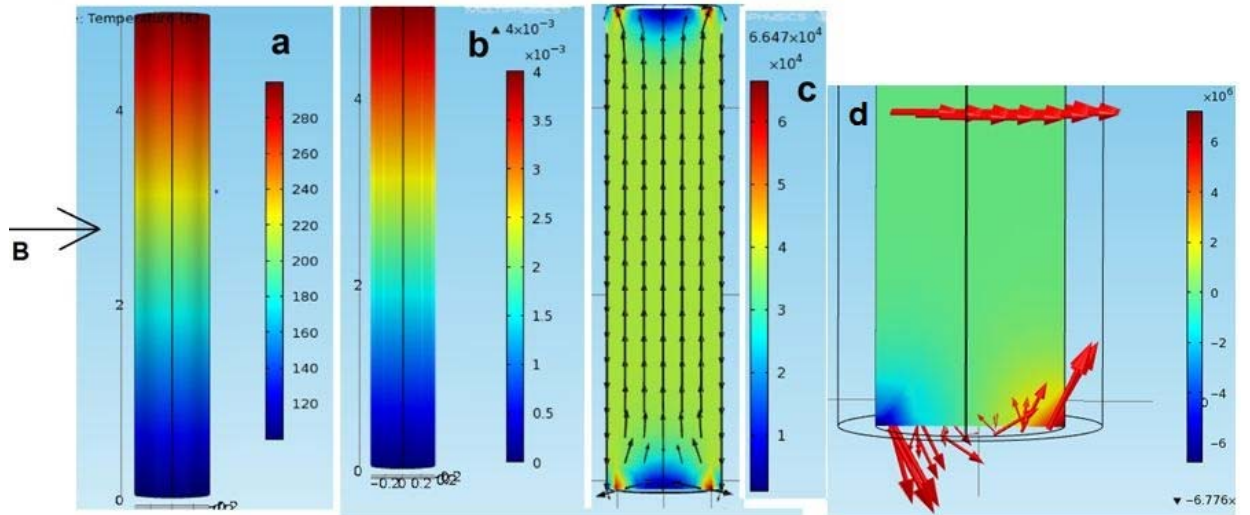
Figure 3.2.5: (a) Temperature distribution in capillary. (b) Electric potential. (c) Electric current. (d) volume force.

Array consisting of 5x5x5 cell 3D mesh (Homogeneous and inhomogeneous heat flows)

Temperature, electric current, potential and force are calculated in liquid lithium surrounding the SS mesh. Domain size is 10x10x10 mm. SS wire diameter is 1mm and mesh sheets are placed 2mm from each other as shown in Figure 3.2.6.a.
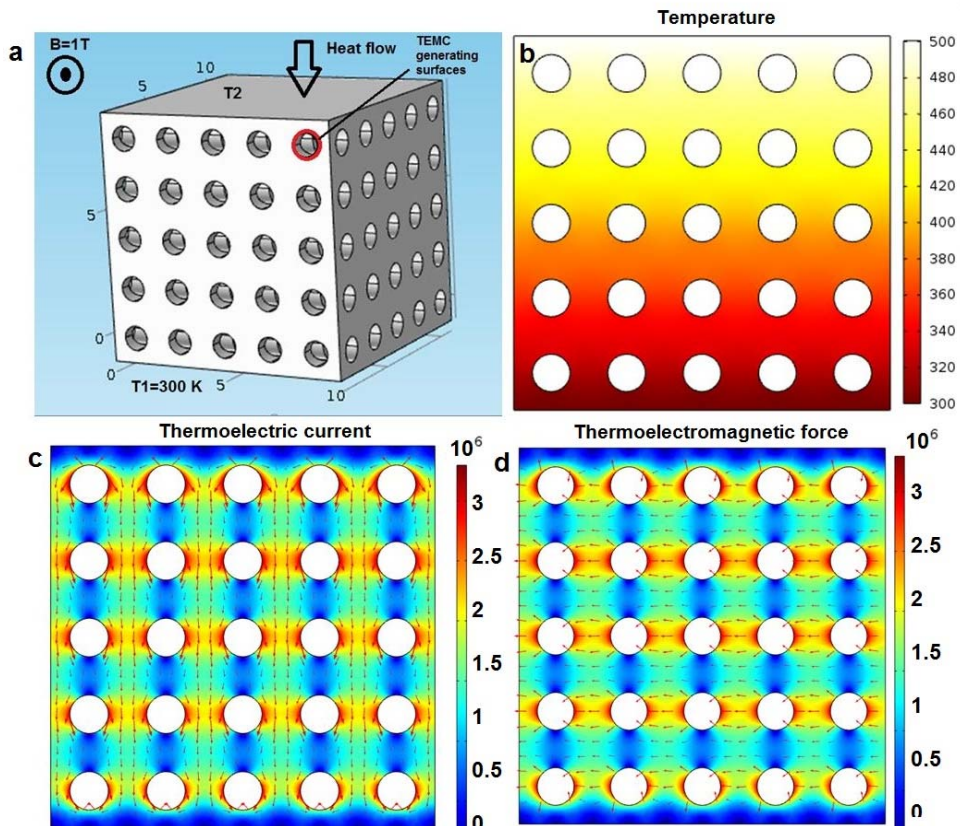

Figure 3.2.6. a) Li/SS mesh with 5x5x5 cells. b) Temperature distribution. c) Thermoelectric current density.

Estimation of current order of magnitude: $j=\sigma \cdot \Delta S \cdot \theta = 3 \cdot 10^6 * 3 \cdot 10^{-5} * 2 \cdot 10^4 = 2 \cdot 10^6$ sim/m agrees well with numerically calculated value in Figure 3.2.6.c. If heat flow is not uniform then force distribution is changed as seen from the results shown in Figure 3.2.7.
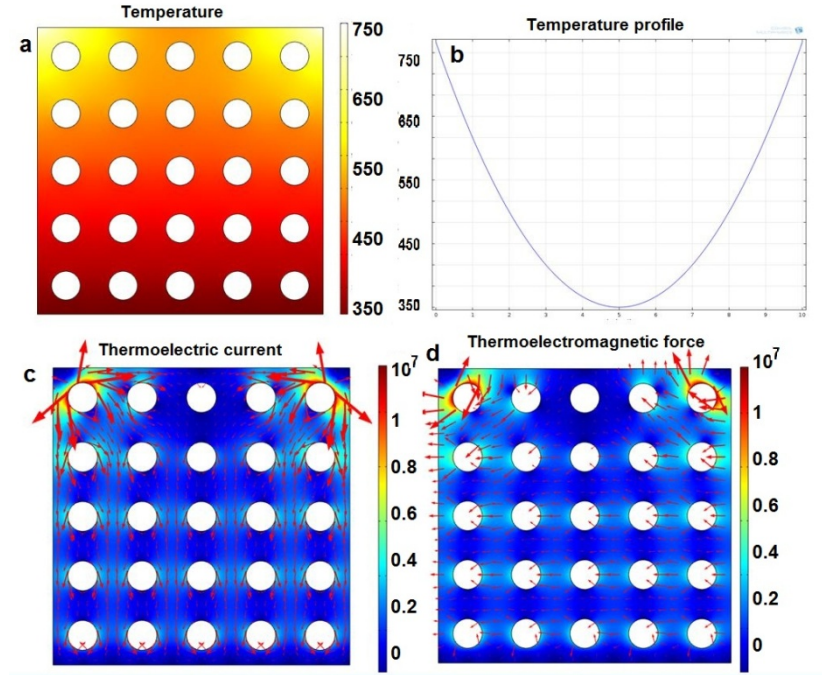

Figure 3.2.7 a) Temperature. b) Temperature profile along top edge. c) Thermoelectric current. d) Thermoelectromagnetic force.

In this case maximum force value is three times higher than with uniform temperature distribution. Force direction and magnitude shows that in this case force may cause surface deformation or push the lithium out of the surface.

$F_{TE}=1*10^7$ N/m^3
$F_g=\rho g=5*10^3$ N/m^3
$F_{capillary}=\gamma/a=0.32/0.001=3*10^3$ N/m^3

Conclusions
Thermoelectric effect is present at the boundaries between two media with different Seebeck coefficients. For a given problem this effect is analyzed for two length scales. First is macroscale TE current flow caused by temperature gradient along CPS/SS boundary. This current interaction with magnetic field creates macroscopic pressure field but does not drive TEMC. Second is TE effects in capillary scale. High temperature gradient (40 K/mm) along capillary causes higher current density. Electric current in liquid Li in the capillary is homogeneous except near the ends of the capillary where current flows through the interface between SS wall and Li. As a result liquid Li flow is induced only near the ends of capillary. Numerical models show that maximum velocity in these regions is 0.8 m/s which is comparable with pressure driven flow (2 m/s).
Numerical simulation of 3 dimensional SS mesh surrounded by liquid lithium shows that in case of inhomogeneous heat flow high local thermoelectric force density may appear. In demonstrated example it is shown how 100 K/mm temperature gradient along the CPS/plasma surface can create up to 10^7 N/m^3 thermoelectromagnetic force which is directed perpendicular to the surface. Thus large local heat pulses may cause forces which deform the surface or expel lithium into plasma.

References

1. D.N. Ruzic, M. A. (2010). *Lithium Walls: The Ultimate Technology.* Illinois: Center for Plasma-Material Interactions. 3rd international symposium on lithium applications for fusion devices. (2013).
2. Davoust, L., Bertrand, F., Moreau, R., Tanguy, P., & Bolcato, R. (1997). Recent results on MHD damped convection in the horizontal Brigman configuration. *Magnetohydrodynamics* (4, pp. 319-327).
3. Gorbunov, L. (1987). Effect of thermoelectromagnetic convection on the production of bulk single crystals consisting of semiconductor melts in a constant magnetic field. *Magnetohydrodynamics* , No. 4, pp. 65-69.
4. Lehmann, P. M., Camel, D., & Bolcato, R. (1998). Modification of interdendritic convection in directional solidification by a uniform magnetic field. *Acta Materialia* , Vol. 46, No. 11, pp. 4067-4079.
5. Polzin, K. (2007). *Liquid-metal pump technologies for nuclear surface power.* Alabama: Marshall space flight center.
6. Shercliff, J. (1979). Thermoelectric magnetohydrodynamics. *Journal of fluid mechanics*, Vol. 91, part 2, pp. 231-251.

3.3. Activity: Armor materials WP13-MAT-HHFM-01-02/ University of Latvia
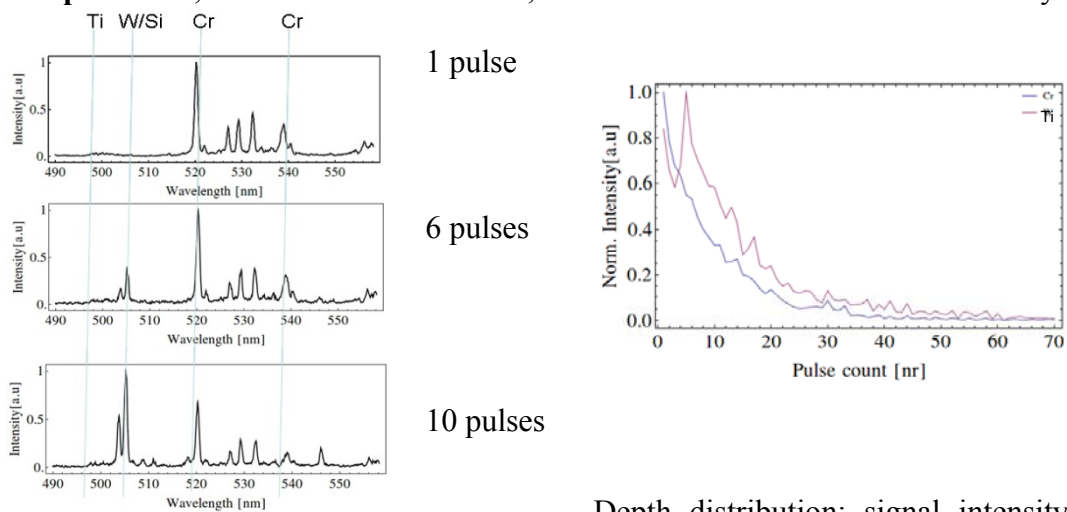**Principal investigator: Dr. I. Tale**
Staff members: A.Voitkans, J. Butikova, B.Polyakov.

Laser-induced breakdown spectroscopy (LIBS) had been performed for the W/Cr/Ti samples on different substrates: sapphire, quartz, and silicon wafer with Cu interlayer. Nd:YAG pumped diode laser with pulse width of 9 ns, repetition rate of 1 kHz, and laser power density of 0.85 J/cm^2 with 1064 nm wavelength has been used for sample ablation. The material ablation rate was in average 7 nm per laser pulse. The samples were ablated in the vacuum chamber with the pressure of 10^{-5} Torr.

The spectral region of 490 – 560 nm has been chosen to be able to detect all the elements of interest in one spectrum. Spectrum of the each pulse has been recorded. The material ablation rate has been derived from the depth of the ablation craters and the number of applied pulses.

The typical results for the samples with different substrates are the following:

Sample K 003; W/Cr/Ti content 83/15/2; substrate: silicon wafer with Cu interlayer.
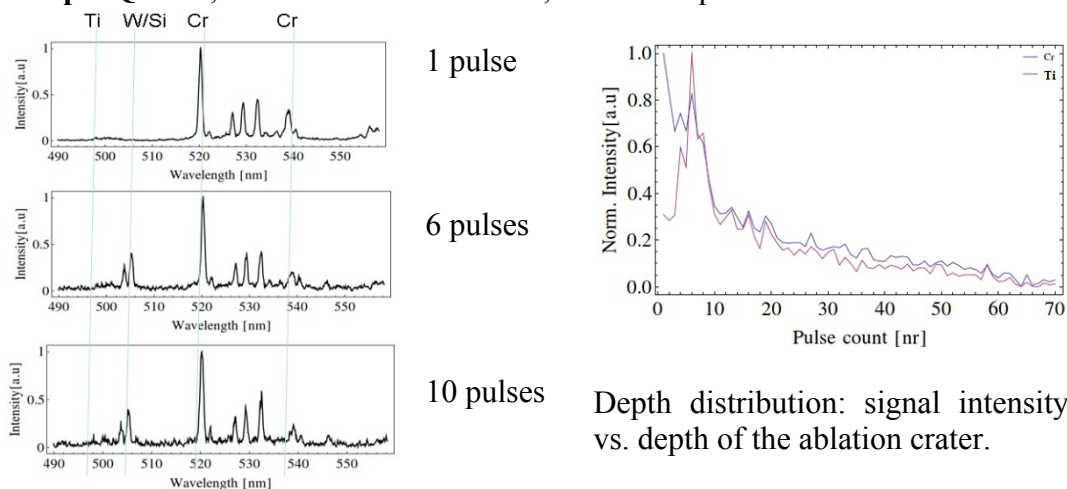

1 pulse

6 pulses

10 pulses

Depth distribution: signal intensity vs. depth of the ablation crater. 1 pulse = 7 nm.

LIBS spectra

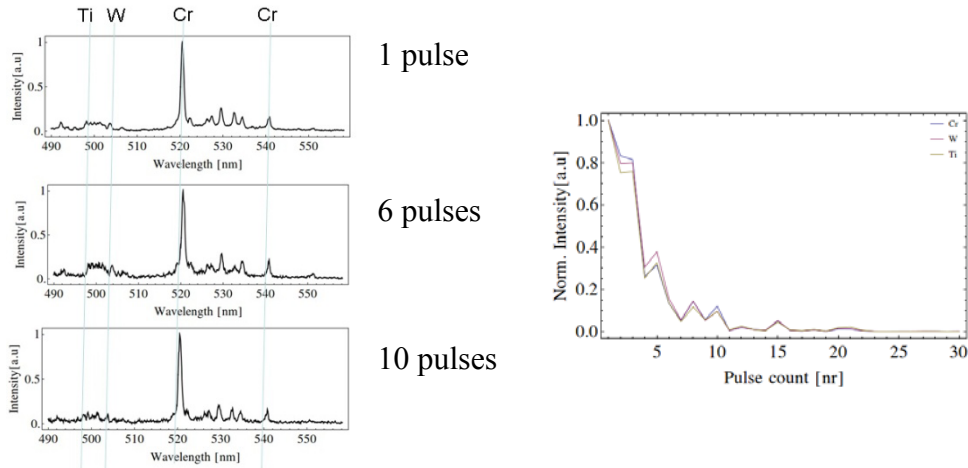**Sample Q 1137**; W/Cr/Ti content 83/15/2; substrate: quartz.

1 pulse

6 pulses

10 pulses

Depth distribution: signal intensity vs. depth of the ablation crater.

LIBS spectra   1 pulse = 7 nm.

During the deposition of these samples, due to the operator error, the top layer of these samples were without of very little W; that's why W has not been included in the depth distribution plot.
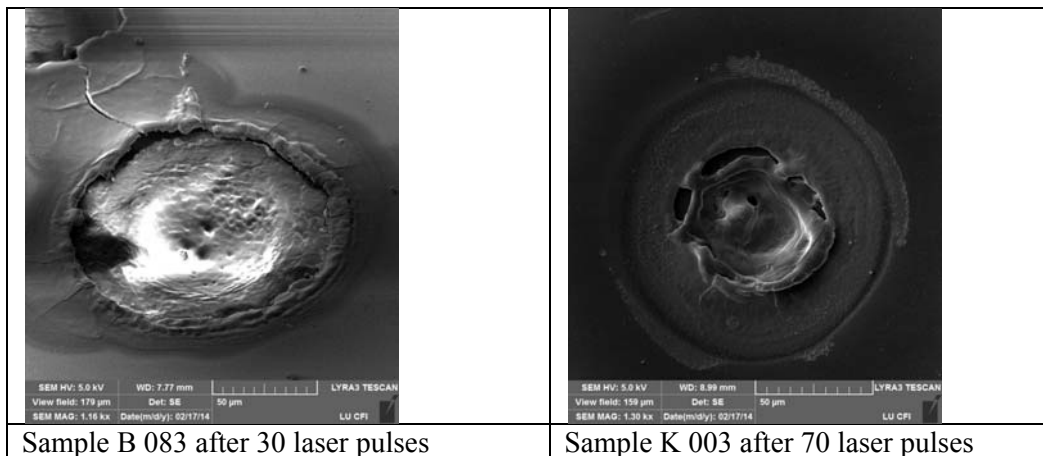
Sample B 083; W/Cr/Ti content 75/15/2; substrate: sapphire.

1 pulse

6 pulses

10 pulses

LIBS spectra

Depth distribution: signal intensity vs. depth of the ablation crater.
1 pulse = 7 nm.

SEM images of the ablation craters

| Sample B 083 after 30 laser pulses | Sample K 003 after 70 laser pulses |

There is an evidence of the boiling and resolidification processes in the both craters, which restricts the accuracy of determination of the ablation rate and element contents.

Conclusions

For the samples with Si-containing substrates, W signal can be easily mixed up with Si in this spectral region. For these samples, the contents of W should be determined in the region where it is not overlapping with other objects of interest.

The decrease of the signals on the depth distribution plots can be explained with unsuccessful choice of geometry of the experiment. The ablation plasma light has been collected on the 90° to the ablation laser beam. Due to the low intensity required for the minimal ablation rate, the plasma plume had disappeared inside the crater forming in the

process of ablation, and the light became undetectable. To avoid such situation, in the future experiments the light will be collected in the direction parallel to the ablation beam.

In order to improve the process of crater formation, it is planned to use defocused picosecond laser beam to increase the diameter of the crater, avoid boiling and increase the resolution of the determination of the element concentrations and material ablation rate.

The future experiments include modelling to determine the quantitative contents of the samples.

3.4. Theory and code development

3.4.1. EU Topical Groups:TG-MHD (MHD), TG-H&CD (Heating and Current Drive)
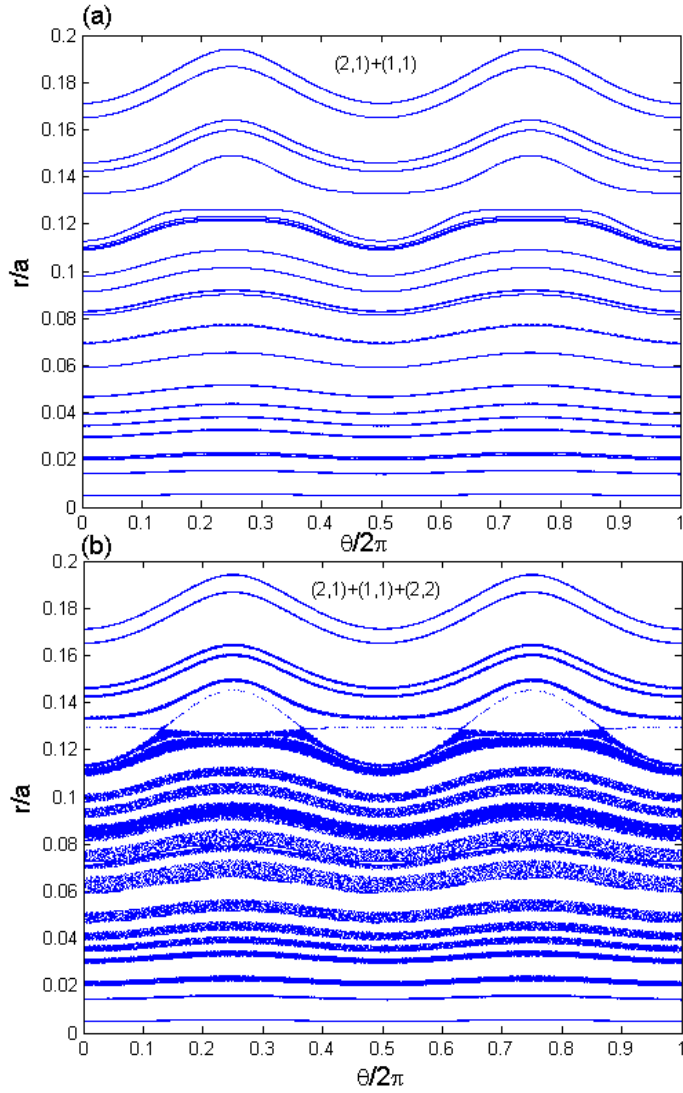
Principal investigator O. Dumbrajs
Research Topics
3.4.1.1.   Bifurcations and fast- slow dynamics in a low-dimensional model for quasi-periodic plasma perturbations

Oscillations of plasma's parameters (sawteeth, edge localized modes (ELMs), frequently interrupted regime of neoclassical tearing modes) are observed when some large scale plasma instabilities do not lead to an immediate termination of a discharge. The understanding of such phenomena is an important tool in controlling the whole reaction. There are many fundamental approaches to the subject, but, despite the huge theoretical and experimental effort, it seems that the phenomena are not fully understood. We focus on a low dimensional model which describes the dynamics of the plasma pressure gradient and of the amplitude of the magnetic field displacement. We study the Hopf bifurcation, analyze the fast-slow dynamics which appears for small normal heat diffusion and we corroborate the results with those observed in experiments.

3.4.1.2.   Mode coupling as an explanation for strong sawtooth-like crashes in the EAST tokamak
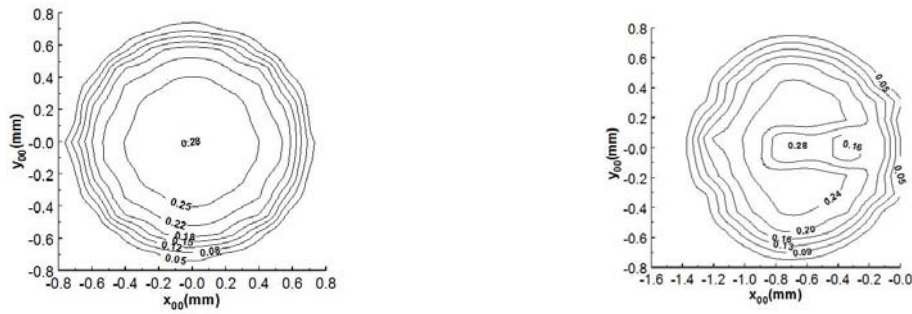
Evolution of the safety factor profile during L-H transition in Experimental Advanced Superconducting Tokamak (EAST) is accompanied by strong central crashes before the regular sawteeth behavior. These crashes appears in the absence of q=1 surface inside the plasma. It was found that the possible explanation is interaction of m/n=1/1 helical mode accompanied by the growth of m/n=2/1 and m/n=2/2 modes (m and n is the poloidal and toroidal mode number, respectively). Contrary to the other cases, here the (2,1) mode with resonant surface inside the plasma interact with (1,1) and (2,1) which have no resonant surfaces (q(0) is higher then 1). Both spatial and temporal characteristics of modes have been analyzed, and in conjunction with the field-lines mapping analysis it was found that the strong crash can be explained by development of a stochastic zone due to the involvement of m/n=2/2 mode.

The Poincare plots: (a) with the input of the m/n=2/1 mode and the m/n=1/1 mode, (b) with the input of m/n=2/1, m/n=1/1, and m/n=2/2 modes. There is only a little excursion in (a) while the stochastic zones are obvious $r/a < 0.14$ in (b). This is exactly in agreement with the region of appreciable big crashes in experiments.

3.4.1.3. Effect of electron beam misalignments on the gyrotron efficiency

The theory describing the operation of gyrotrons with tilted and shifted electron beams has been developed. Effects of the tilt and shift are studied for a 1 MW, 170 GHz gyrotron, which is presently under development in Europe for electron cyclotron resonance plasma heating and current drive in the International Thermonuclear Experimental Reactor (ITER). It is shown that one should expect significant deterioration of gyrotron operation in such gyrotrons when the tilt angle exceeds 0.4-0.5° and the parallel shift of the beam axis with respect to the axis of a microwave circuit is larger than 0.4-0.5 mm. At the same time, simultaneous tilting and shifting in a proper manner can mitigate this deteriorating effect.

Efficiency as a function of transverse coordinates in the cases of (a) parallel displacement, (b) a tilt angle 1°.

Collaborators

K. Chen (Institute of Plasma Physics, Chinese Academy of Science, **China**)
D. Constantinescu (Faculty of Exact Sciences, University of Craiova, **Romania**)
Liqun Hu (Institute of Plasma Physics, Chinese Academy of Science, **China**)
V. Igochine (Max-Planck Institut für Plasmaphysik, Assotiation Euratom-IPP,
        Germany)
K. Lackner (Max-Planck Institut für Plasmaphysik, Assotiation Euratom-IPP,
        Germany)
Erzhong Li (Institute of Plasma Physics, Chinese Academy of Science, **China**)
G.S. Nusinovich (University of Maryland, **USA**)
T. Shi (Institute of Plasma Physics, Chinese Academy of Science, **China**)
L. Xu (Institute of Plasma Physics, Chinese Academy of Science, **China**)
H. Zohm (Max-Planck Institut für Plasmaphysik, Assotiation Euratom-IPP,
        Germany)

Publications

1. D. Constantinescu, O. Dumbrajs, V. Igochine, K. Lackner, and H. Zohm *"Bifurcations and fast- slow dynamics in a low-dimensional model for quasi-periodic plasma perturbations"* Romanian Physics Report (in print).

2. Erzhong Li, V. Igochine, O. Dumbrajs, L. Xu, K. Chen, T. Shi, and L. Hu *"Mode coupling as an explanation of strong sawtooth-like crashes in the EAST tokamak"* Plasma Phys. Control. Fusion (in print).

3. O. Dumbrajs and G.S. Nusinovich *"Effect of electron beam misalignments on the gyrotron efficiency"* Phys. Plasmas **20**, 073105 (2013).

Conferences

1. 40th European Physical Society conference on plasma physics, July 1-5, 2013, Espoo, Finland.
2. 38th International Conference on Infrared, Millimeter and Terahertz Waves, September 1-6, 2013, Mainz, Germany.

3.4.2. Progress Report on AEUL activity (4.2. part, Materials Modeling) in 2013-2014

Coordinator: Prof. V.N. Kuzovkov
Ab initio **atomistic calculations of the reduced activation steels strengthened by yttrium oxide precipitates**
Principal investigator: E.A. Kotomin,

Yu.F. Zhukovskii, Yu.A. Mastrikov, A. Gopejenko,
Collaboration: Dr. A. Möslang and Dr. P.V. Vladimirov (IAM, Karlsruhe Institute of Technology, Germany)

Problem:

Reduced activation steels strengthened by yttria precipitates are considered as promising construction materials for fusion- and advanced fission-reactors. In particular, their use for fusion reactor blanket structure leads to increase of the operation temperature by ~100°C. Both size and spatial distributions of Y_2O_3 nanoparticles drastically affect both mechanical properties and radiation resistance of ODS steels. Further optimization of the manufacture process requires a deep understanding of atomic scale mechanism for growth of oxide nanoparticles. Meanwhile, it is still unclear.

To solve this problem, we perform large-scale computer simulation of the yttrium and oxygen precipitation in both *bcc*- and *fcc*-Fe lattices containing single and multiple Fe vacancies, which is necessary for understanding the basic mechanisms of processes involved in ODS steel production. To this end, we are performing *ab initio* study of kinetic parameters for yttrium and oxygen precipitation necessary for a first stage of multi-scale modelling approach aimed at investigation of the role of various solute elements on the precipitation kinetics.

Method:

The first principles calculations on the kinetic parameters of yttrium and oxygen precipitation in both iron lattices: α-Fe (low-temperature phase) and γ-Fe (stable at high-temperature), can be considered as a *first stage* of multi-scale modeling aimed at clarification of the role of various solute elements in this process. It includes supercell models of single Fe vacancies, O and Y impurity atoms as well as their aggregates in the α- and γ-Fe lattices, in order to estimate the corresponding pair-wise interactions and energy barriers for migration of impurities inside each lattice. Both interaction energies between solute and matrix atoms and barriers for migration of different solute atoms can be extracted from the first principles calculations and used then for atomistic kinetic Monte Carlo simulations of Y_2O_3 nanoparticle formation, a *second stage* of multi-scale modeling.

The latter implements the lattice kinetic Monte Carlo (LKMC) method for simulations on the matrix and interstitial sublattices, in order to study the precipitate growth. For Fe atoms and substitution solutes (Y atoms), the sublattice matrix is used only, while the O atom can reside inside both the octahedral and tetrahedral interstitial sublattice sites as well as the vacancies. Migration of yttrium atom may occur only in the case of necessary concentration of vacancies, the absence of which can result in a wrong description of the kinetics of precipitate growth. Diffusion of precipitates occurs inside the matrix lattice and structures of some precipitates are coherent with it. With further growth of precipitates, their interaction with matrix becomes less important than the precipitate bulk energy. This might result in the phase transition of precipitates to the more stable phase, *i.e.*, their coherence with the matrix can be lost.

Progress in 2013-2014

Y diffusion barriers were calculated for different diffusion trajectories using NEB band method. In order to improve the precision of diffusion barrier energy up to 7 intermediate

configurations were calculated which required up to 1792 CPUs. Fig.3.4.2.1. illustrates initial and final configurations diffusion trajectory.
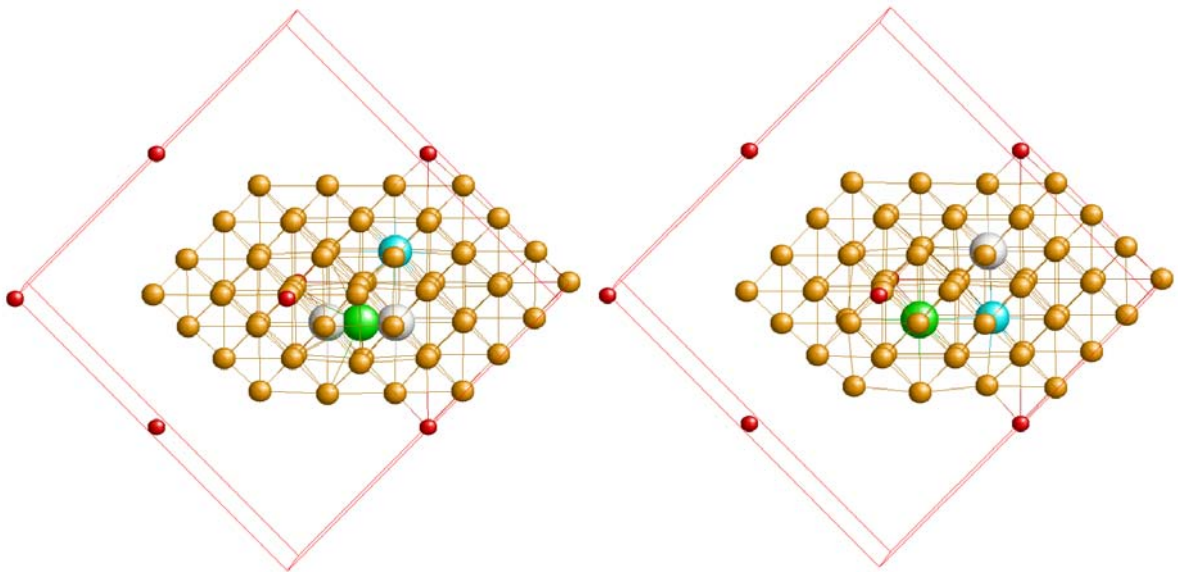

Fig.3.4.2.1. Initial and final configuration for the Y diffusion path.

Diffusion barriers for Y at different distances with Fe atom are shown in Table 1. Quite high diffusion barrier energies indicate that increased concentration of vacancies is required for Y to diffuse faster.

Table 1. Y diffusion barrier energies

Configuration	E_{bind}, eV*
Y-Fe (1-NN)	2.60
Y-Fe (2-NN)	2.37
Y-Fe (3-NN)	1.85
Y-Fe (4-NN)	1.81

Fig.3.4.2.2. illustrates the necessity of performing diffusion barrier calculations with a large number of intermediate configurations. As it is clearly seen some diffusion path are non-symmetrical so in some cases diffusion barrier may deviate from the center point.
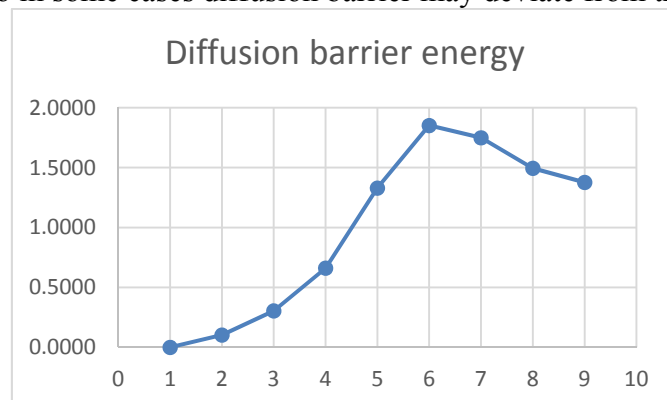

Fig.3.4.2.2. Diffusion barrier energy

In order to increase the concentration of vacancies it is necessary to increase the supercell size. This is required to decrease the interaction between periodical images of the defects. However, this also requires additional test calculations to check if the results received for the larger supercell reproduce the results received earlier for the smaller supercell.

Table 2. Bonding in Y_{Fe}-V_{Fe} pairs in γ-Fe

Supercell	4×4×4	5×5×5
Configuration	E_{bind}, eV*	E_{bind}, eV*
1-NN	1.67	1.42
2-NN	-0.21	-0.07
3-NN	0.30	0.14
4-NN	0.40	0.30

Table 2 shows the comparison of the results of Y-V binding energies received for 4×4×4 64 atom supercell and 5×5×5 125 atom supercell. As it is seen from the table the results are in a good qualitative agreement. In all cases only the absolute vaues of the binding energies decreased which can be explained by the reduced interactions of defect periodic images which is the main goal of the calculations with larger supercell.

The mechanisms of Y-V-Y complex migration in the *bcc*-Fe matrix have been studied by modelling the most energetically stable configurations (Fig.3.4.2.3) and the transition states between them.

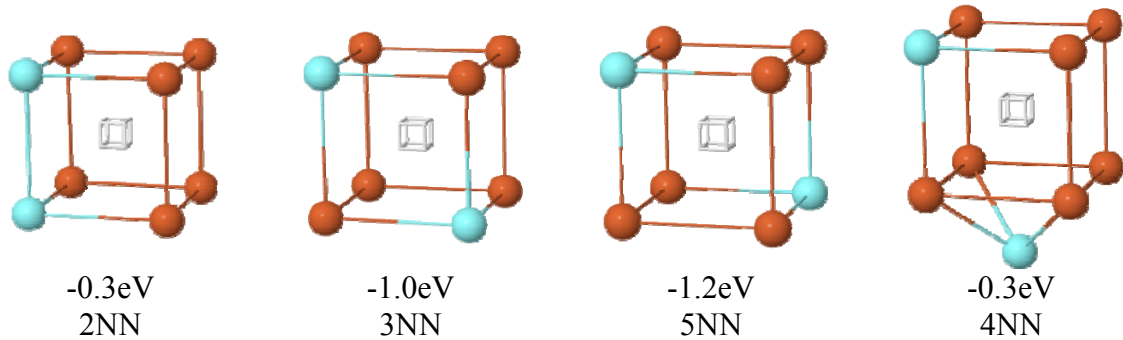| -0.3eV | -1.0eV | -1.2eV | -0.3eV |
| 2NN | 3NN | 5NN | 4NN |

Fig. 3.4.2.3. The most stable configuration of the Y-V-Y complex.

The attraction between two Y solute atoms is the strongest at the 5NN distance. Beside single jump of vacancy, we have proposed a more complex migration mechanism, which allows transformation of the Y-V-Y complex. The process consists of two simultaneous jumps V and Y solute atom. Monovacancy jumps along <111>, whereas Y atom jumps along <001>and<111> (Fig.3.4.2.4) . Y, switching sites with Fe atom, jumps into one regular site, and then continue moving, until it reachs another regular site. By this two-step mechanism most of the stable states can be directly transformed one into another. A complete set of the transition states of the complex realisticly describes the process of the migration of the Y-V-Y cluster in the *bcc*-Fe matrix.

Calculation of the transition states have been performed using six intermediate images on the IFERC-CSC computer Helios, which results in 98000 CPU*hours.

Obtained data have been compiled into the unified database for the further treatment. The master replica of the database is stored at the KIT.
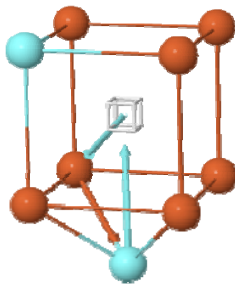
Fig.3.4.2.4. Two-step migration mechanism of the Y-V-Y complex. Y jump along the [001] and [111], combined with V jump along the [11-1]. Initial state 4NN, final -3NN (Fig.3)

Presentations:

1. *29th ISSP Conference (Riga, Latvia, February, 2013).*
A. Gopejenko, Yu.F. Zhukovskii, P.V. Vladimirov, E.A. Kotomin, J.Mastrikov, and A. Möslang, "*Ab initio* calculations of Y and vacancies interactions in fcc Fe lattice". Abstracts: p. 61.

2. *11th International Conference "Information Technologies and Management", IT&M'2013 (Riga, Latvia, April, 2013).*
A. Gopejenko, Yu.F. Zhukovskii, P.V. Vladimirov, E.A. Kotomin, Yu.A. Mastrikov, and A. Möslang, "First principles modeling of interactions between Y, O and vacancies in *fcc*-Fe lattice". Abstracts: p. 112-114.

3. *9th International Conference "Functional Materials and Nanotechnologies" FM&NT-2013 (Tartu, Estonia, April, 2013).*
Yu.F. Zhukovskii, A. Gopejenko, Yu.A. Mastrikov, E.A. Kotomin, P.V. Vladimirov, and A. Möslang, "Modeling of Y-O precipitation in *bcc*-Fe and *fcc*-Fe lattices." – Abstract: OR-35.

4. *Annual Monitory Meeting of European Fusion Development Agreement, EFDA - 2013 (Bucharest, Romania, June, 2013).*
Yu.A. Mastrikov, P.V. Vladimirov, V.A. Borodin, Yu.F. Zhukovskii, E.A. Kotomin, and A. Möslang, "*Ab initio* modeling of nY/nV_{Fe} complexes diffusion in the α-Fe lattice."

5. EFDA MAT – IREMEV Monitoring Meeting, (Garching, Germany, February 2014) Yu.A. Mastrikov, P.V. Vladimirov, V.A. Borodin, Yu.F. Zhukovskii, E.A. Kotomin, and A. Möslang "*Ab initio* modeling of the 2Y/3V cluster migration in the *bcc* Fe lattice."

6. *30th ISSP Conference (Riga, Latvia, February, 2014).*
A. Gopejenko, Yu.F. Zhukovskii, P.V. Vladimirov, E.A. Kotomin, Yu.A Mastrikov, V.A. Borodin and A. Möslang, "First principles calculations of the energy barriers for different trajectories of Y atom migration inside *fcc*-Fe lattice". Abstracts: p. 36.

7. *12th International Conference "Information Technologies and Management", IT&M'2014 (Riga, Latvia, April, 2014).*
A. Gopejenko, Yu.F. Zhukovskii, P.V. Vladimirov, E.A. Kotomin, Yu.A. Mastrikov, V.A. Borodin and A. Möslang, "*Ab initio* calculations of interactions between Y, O impurity atoms and Fe vacancies for ODS steel implementation in fusion reactors". Abstracts: p. 21-22.

4. EFDA FUSION TECHNOLOGY PROGRAMME

4.1. INVESTIGATION OF FUEL RETENTION IN VARIOUS JET TILES

Principal investigator: **G.Kizane**
M. Halitovs, L. Avotina, L. Baumane, J. Jansons, J. Lapins

The accumulation of fusion fuel in the vacuum vessel materials of fusion devices, especially in a divertor region, has always been one of the major problems for various fusion devices. In order to reduce the fuel retention the constructions as well as materials of a divertor are constantly upgraded.

Tungsten W coating for carbon fibre composite (CFC) material is proposed as the latest upgrade for pure CFC material divertor used in JET. The $15 - 25$ μm W coating with molybdenum Mo or rhodium Rh interlayers are meant to decrease the sputtering of plasma facing materials and to decrease accumulation of fusion fuel on the surface and in the bulk of divertor materials.

The task of the EFDA JET Technology project JW13-FT-1.21 "AMS and FCM + LSC Investigation of Fuel Retention in Various JET Tiles" is estimation of influence of tungsten layer on a surface of a tile on tritium accumulation, on a profile of tritium. The project was realized in cooperation with EURATOM associations of Romania, MEdC and Finland, TEKES.

Analysed tiles are from the JET campaign 2007 – 2009 of divertor MkII-HD and from the campaign 2010 – 2012 of divertor MkII-HD ILW. Samples from tungsten non-coated tiles are following - MkII-HD divertor – 2BNG4C, 2BNG6D, 2ONG7A and 2ONG8B. Samples from tungsten coated tiles of divertor MkII-HD (ITER Like Wall)-2BNG6C, 2ONG7A*, 2ONG8B* (* further in the text means that samples are from campaign 2010-2012).

Determination of tritium in a separate sample was realized by standard full combustion and liquids scintillation method. To determine the total amount and location of tritium within tiles, several sample cylinders were drill-holed and sawn in slices of approximately 1 mm thickness. The slices were used in full combustion method (FCM) and the amount of tritium in oxidation products was determined by liquid scintillation counting (LSC). The activity of tritium was calculated per gram of the sample and per 1 cm^2 of the plasma facing surface.
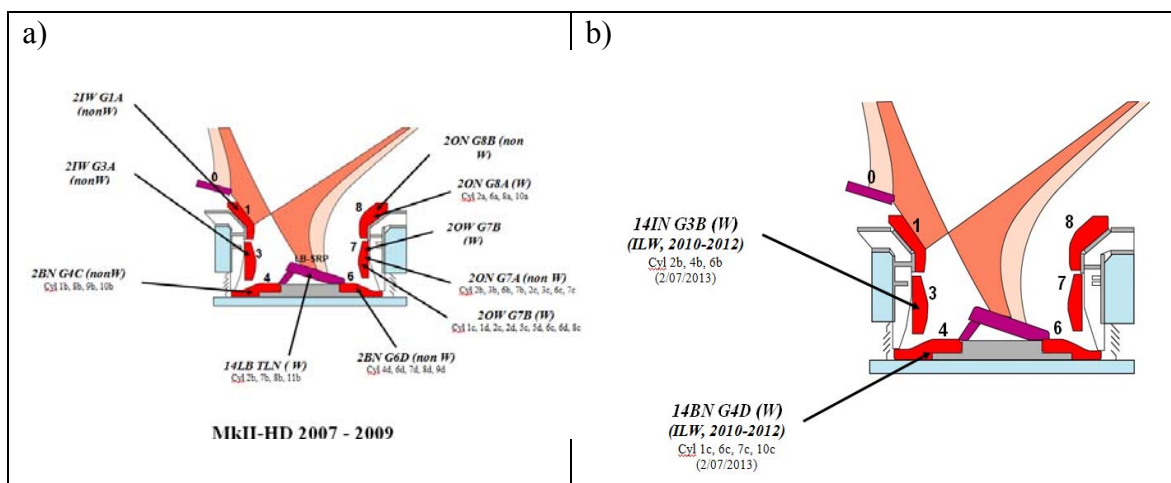

Fig. 4.1.1 Cross-section of the divertor MkIIHD and analysed tiles: a) campaign 2007-2009, b) 2010-2012.

Comparison of tritium accumulation in W-coated (200 μm tungsten coating for 2007 - 2009 or ~ 25 μm tungsten coating for 2010 - 2012 samples with molybdenum or rhodium interlayer) and non-coated CFC tiles of JET divertors was made. As tungsten has higher density and is less affected by sputtering than carbon, it should decrease the total amount of accumulated tritium and prevent its transport in the tiles.

Samples of vertical tile 14ING3B top layer have tritium mass activity of $(0.13 \div 0.21) \cdot 10^5$ Bq·g^{-1} whereas horizontal "floor" tile 14BNG4D sample activity increases from $0.15 \cdot 10^5$ Bq·g^{-1} to $0.37 \cdot 10^5$ Bq·g^{-1} towards the central load-bearing tile of the divertor.
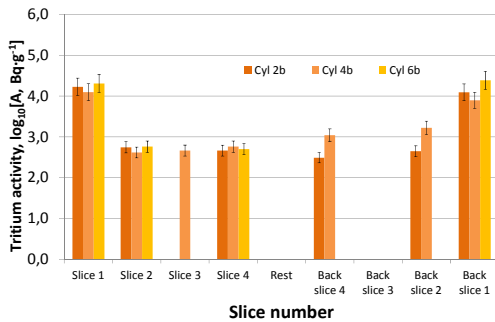

Fig. 4.1.2 Tritium mass activity in Tile 14ING3B (W-coated, ILW, 2010-2012) cylinders Cyl2b, Cyl4b and Cyl6b (combusted in 2013)
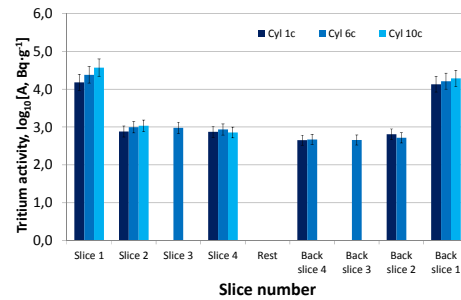
Fig. 4.1.3 Tritium mass activity in Tile 14BNG4D (W-coated, ILW, 2010-2012) cylinders Cyl1c, Cyl6c and Cyl10c (combusted in 2013)

The bulk activity of 14ING3B and 14BNG4D tile samples gradually decreases until roughly 1 mm in depth of tile and remains constant at $(0.46 \div 0.56) \cdot 10^3$ Bq·g^{-1}.
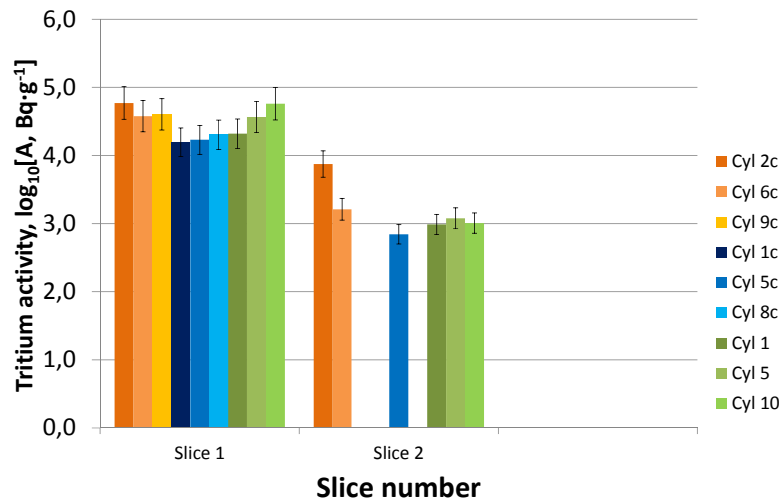

Fig. 4.1.4 Tritium mass activity comparison
Tile 2BNG6C (W-coated, ILW); cylinders Cyl2c, Cyl6c and Cyl9c,
Tile 2ONG7A (W-coated, ILW); cylinders Cyl1c, Cyl5c and Cyl8c
Tile 2ONG8B (W-coated, ILW) cylinders Cyl1, Cyl5 and Cyl10
(combusted in 2013), JET MkII-HD ILW divertor (2010 - 2012)

The W-coated tile 2BNG6C has a homogeneous surface tritium activity with average values being $4.7 \cdot 10^4$ Bq·g^{-1} and bulk activity – $4.6 \cdot 10^3$ Bq·g^{-1}.

Samples of W-coated tile 2ONG7A* has average surface tritium activity $1.8 \cdot 10^4$ Bq·g^{-1} with bulk tritium activity of 10^3 Bq·g^{-1} level.

W-coated tile 2ONG8A* show average activity of $5 \cdot 10^4$ Bq·g^{-1} at the top layer and approximately the same bulk activity as in tile with no tungsten coating – $3 \cdot 10^3$ Bq·g^{-1}.

The obtained results for non-covered CFC tile 2BNG4C show that average surface tritium activity is in rage of $(0.7 \div 6.7) \cdot 10^5$ Bq·g^{-1} while volume activity is at a level of $3.7 \cdot 10^3$ Bq·g^{-1}.
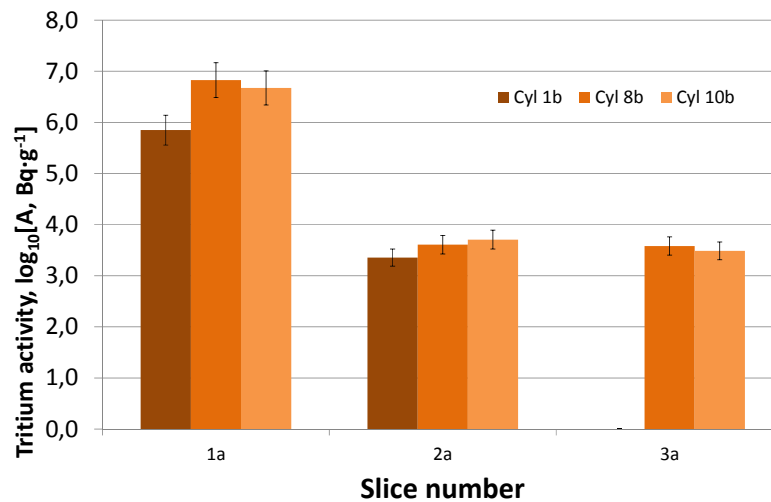

Fig. 4.1.5 Tritium mass activity comparison in:
Tile 2BNG4C (non W-coated); cylinders Cyl1b, Cyl8b, Cyl10b, combusted in 2013, JET MkII-HD divertor (2007 - 2009)

For the floor tile 4 it can be concluded that by coating divertor with W coating, surface activity reduced by a factor of 20, also reducing bulk tritium activity by more than 4 times. As a result of less divertor material erosion and further tritium accumulation in erosion materials, bulk activity is also diminished as the total amount of tritium on the surface layer available for volume diffusion processes is reduced.

For the divertor floor tile 6, being in a "shadowed" zone of direct plasma interaction, accumulation of erosion materials on the surface is of a great importance. Tile with no coating 2BNG6D had average surface tritium activity $5.5 \cdot 10^5$ Bq·g^{-1} rapidly changing by a factor of 30 for samples in "open" part of the tile to "shadowed" part where direct plasma has almost no interaction with the tile surface.

As for tile 7, the non-coated tile 2ONG7A has average surface tritium activity $5.4 \cdot 10^4$ Bq·g^{-1} with bulk tritium activity of $1.7 \cdot 10^3$ Bq·g^{-1}.
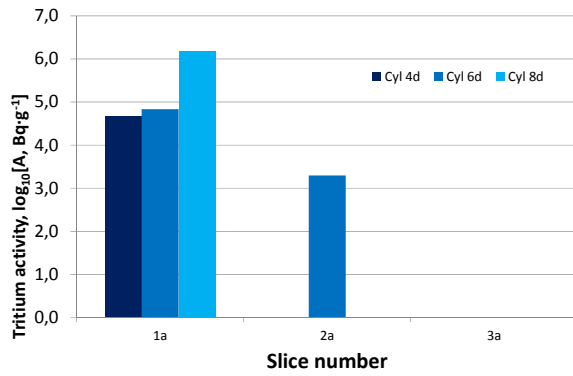
Fig.4.1.6 Tritium mass activity comparison in: Tile 2BNG6D (non W-coated)
cylinders Cyl4d, Cyl6d, Cyl8d,
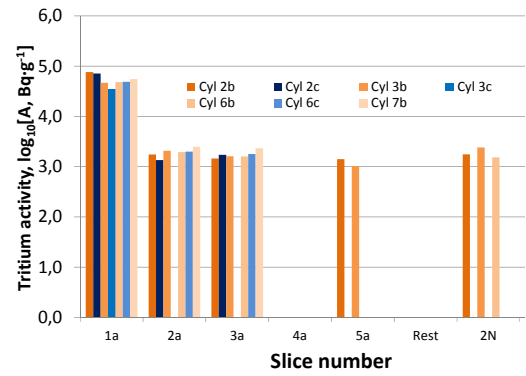combusted in 2013
JET MkII-HD divertor (2007 - 2009)

Fig. 4.1.7 Tritium mass activity comparison in Tile 2ONG7A (non W-coated)
cylinders Cyl2b, Cyl2c, Cyl3b, Cyl3c, Cyl6b, Cyl6c, Cyl7b,
combusted in 2013
JET MkII-HD divertor (2007 - 2009)

W coating reduces the total amount of tritium collected, but the effect is much less significant than for tile 4 being under more frequent plasma interaction during fusion, the bulk activity remains almost the same. Therefore it could be concluded that kinetic collision-like tritium access through the surface of divertor tiles is much less influent for the bulk activity. It can be assumed that tritium bulk activity levels are mainly driven by diffusion processes rather than a rapid kinetic process during the plasma interaction with the divertor.

The reducing effect of tritium accumulation is even smaller for the tile 7 samples. While coating slightly decreases the tritium surface activity for a tile that has small direct plasma-facing surface interaction time, the bulk activity remains similar to previously described tiles.

Fig. 5.1.8. Tritium activity in depth of divertor tile 4 (x indicate tile 2BNG4C samples, o indicate 14BNG4D samples)

Fig. 4.1.9 Tritium activity in depth of divertor tile 7 (x indicate tile 2ONG7A samples, o indicate 2ONG7A* samples)

As observed in previous researches, the difference of tritium activity in the upper layer of divertor can reach even the magnitude of 5 powers with average bulk activity level of 10^4 Bq·g^{-1}. While tungsten-coated materials as showed have a steady difference of less than 2 magnitudes with slightly lower bulk activity ($3 \cdot 10^3$ Bq·g^{-1}).

W coating is unarguably effective in reducing tritium accumulation on the surface and in the bulk of divertor tiles. It is clearly shown in performed experiments that tungsten coating decreases the accumulation of tritium in the top layer. This is due to smaller penetrability of tungsten for tritium and lesser sputtering material in which tritium has been previously collected on carbon fibre composite divertor tiles. The efficiency of this process varies and the best results would be achieved for the tiles that have more plasma-facing surface interaction time and higher energy load. The research also shows that W coating barely affects the tritium bulk activity and most likely comparably slower processes of diffusion are happening that would need detailed studies.

4.2. Preparation for the analysis of long chain hydrocarbon in JET flake/dust material using TGA/DTA coupled to QMS & FTIR

Principal investigator: **G.Kizane**
L. Avotina, L. Baumane, M. Halitovs, D. Conka, J. Jansons, J. Lapins

Materials of the plasma facing wall and divertor of Joint European Torus (JET) until 2009 partially were made from carbon fibre composites (CFC).

During plasma operations, plasma-wall interaction causes erosion, transport and deposition of first wall material to the divertor, leading codeposits, dust and flakes which can contain tritium and build-up an inventory. In the JET 2009 shutdown the analyses of the released gas trapped by the cryopanel with gas chromatography showed presence of hydrocarbons from methane up to nonane (C_9). The fact that hydrocarbons up to C_9 have been found does not preclude the formation of even higher species and indicates that long-chain hydrocarbons or compounds with fullerene-like properties could be present in deposits, dust or flakes from the JET vacuum-vessel.

The presence of long-chain hydrocarbons and fullerenes would be an additional source of tritium retention in a fusion device with materials containing carbon.

The goal of the EFDA JET task JW13-FT-1.23 "Preparation for the analysis of long chain hydrocarbon in JET flake/dust material using TGA/DTA coupled to QMS & FTIR" is to analyse and compare properties of decomposition of dust/flakes, fullerene C_{60}, n-eicosane, n-triacontane, n-tetracontane, pentacontane and hexacontane in inert and in air atmosphere in order prepare to analyse real plasma exposed samples from JET vacuum vessel containing tritium and other impurities.

In the year 2013 analysis of inactive carbon dust prepared from whole inactive carbon fibre composite (CFC) tile, fullerene C_{60}, separate long chain hydrocarbons and mixtures prepared from inactive CFC dust with additions of long chain hydrocarbons, as well as analysis of real deposited and collected carbon dust from the JET vacuum vessel inner divertor "Pot D" of the year 2010 were realized.

The inactive Joint European Torus (JET) dust sample was prepared from a carbon tile. From an inactive JET carbon tile that was not installed in JET machine and thus contained no tritium and no beryllium, 1.5 mm thick slices were mechanically cut with a saw and then broken up to simulate flakes removed/recovered from JET machine. Different sizes of flakes and associated dust were collected. The dust resulting from the flake preparation was collected for analysing in University of Latvia.

High purity substances for mixtures were delivered by Sigma-Aldrich. The delivered substances were an allotrope of carbon fullerene C_{60} (sublimed 99.9%) and five long-chain hydrocarbons with 20-60 carbon atoms in chain: n-Eicosane (99.9%), n-Triacontane (99.1%), n-Tetracontane (99.2%), Pentacontane (99.9%) Hexacontane (99.9%). The active dust sample was collected from JET inner divertor, "Pot D" in 2010.

Used methods for analysis of inactive dust material were optical microscopy, scanning electron microscopy (SEM) Hitachi S-4800, 15 kV_{acc}, 15 μA, energy dispersive X-ray spectrometry (EDX), Quantax Esprit 1.9., Raman, Fourier transform infrared (FT-IR) and electron spin resonance (ESR) spectroscopy, X-ray diffraction (p-XRD) and thermogravimetry complementary with differential thermal analysis (TG/DTA).

Photos were taken through microscope Leica L2, with camera NikonD80. The FT-IR spectra were recorded using a Perkin Elmer Spectrum BX (4000 cm^{-1} to 450 cm^{-1}) spectrometer with a resolution 4 cm^{-1}. Samples for FT-IR analysis were pressed in

potassium bromide pellets. Raman spectra were obtained with Renishaw InVia Raman spectrometer, λ=514 nm, exposure time 25 s, enlargement 50, spot size 2 μm, X-ray diffraction patterns were recorded using a Bruker D8 Advance diffractometer (Δ2Θ = 0.001°, CuKα radiation, 40 kV voltage, 40 mA current, step 0.02°, time per step 0.5 s, 2Θ scale from 10° to 60°). Thermal treatment was performed using thermogravimeter, differential thermal analyzer SEIKO EXSTAR6300 (horizontal differential balance weight measurement method, temperature range room temperature up to 1600K, TG measurement range ±200 mg (0,2 μg), DTA measurement range ±1000 μV (0.06 μV), DTG measurement range 0.5 mg/min ~ 1 gmin^{-1}).

Analysis of inactive JET dust material show that particle size in CFC dust material varies from nanometer size up to hundreds of micrometers. The shape of particles was characterized using SEM. The particles can be divided in two groups: separate particles and non-separated. The 'non-separate' particles are more than 100 μm large parts of CFC tile material, containing fibers. The separate particles are as flakes, particles of irregular shape and cylindrical type particles. There are two types of cylindrical particles. One type of cylindrical particles is with rough surface and diameter more than 10 μm and the others are with smooth surface and diameter below 10 μm. The length of cylindrical particles varies around 10-100 μm.

The particles of irregular shape are also with smooth and rough surface. Size of such particles varies from few to several tens of micrometers. The smallest particles are flake like with a size below 1 μm. The variety of shape and size of particles is in wide range and can represent the dust and flakes formed in the vacuum vessel of JET reactor.

The inactive dust material was analysed with infrared and Raman spectroscopy. In FT-IR spectra in a region 900-1000 cm^{-1} is a broad signal of C=C double bond. Signals in the spectra around 2850-3000 cm^{-1} show a presence of sp^3 hybridized carbon bonds representing signature of sp^3 aliphatic groups. Symmetric deformation vibration of CH$_3$ groups appears at around 1455 cm^{-1}. In spectrum of inactive CFC dust material this signal is close to background level. The presence of graphite as the main phase was approved by Raman spectroscopy. In the Raman spectra of CFC dust material the most intensive is a peak at 1580 cm^{-1}. This peak, called G-band (from Graphite), is due to the bond stretching of both aromatic and aliphatic C-C pairs. A broad peak at 1350 cm^{-1}, D-band (Disorder-related) is due to the breathing of aromatic rings and/or the presence of disorder. One more band that appears in case of disordered graphite is a D'-band at ca. 1620 cm^{-1}. In Raman spectra of inactive CFC dust the D'-band is observed as a shoulder of G-band. The centre of D'-band (1617 cm^{-1}) was obtained by fitting the Raman spectrum with three Lorentz peaks. The ratio between intensities of D- and G-band (I$_D$/I$_G$) is one of several parameters used to characterize the material – as larger is the value of intensity ratio as more disordered is the material. For CFC dust the I$_D$/I$_G$ value is not closing to one, it is 0.32 meaning that the material consists mostly from well-structured graphite with the disordered structures for examples on the edges of crystallites. In p-XRD pattern in 2Θ range from 20º to 60º graphite reflexes are observed. The 002 diffraction peak was fitted with a Gaussian line. Asymmetry observed for 002 diffraction peak is probably due to both fibre particle and pyrolitic components. Position of 002 maxima 26.32º. The interplane distance is deduced from the position by the diffraction relation and for the inactive dust d=0.338 nm That is not differing much from expected graphite value of 0.335 nm, showing that the crystalline part of CFC dust material consists mostly from graphite. The linear dimension of the particles calculated from Scherrer relation is 330 Å. A reference ESR spectrum was taken for the inactive CFC dust materials and the obtained g-value 2.001 is close to a free electron g-value. No other signals were observed showing that material contains no other paramagnetic centres.

The thermal properties of the inactive CFC dust material were investigated with thermogravimetry (TG) in combination with differential thermogravimetry (DTG) and differential thermal analysis (DTA). The samples were heated with controlled heating rate in inert and air atmosphere. The slow heating rates (0.5; 1 $Kmin^{-1}$) allowed following precisely to mass changes, faster heating rates (5 and 10 $Kmin^{-1}$) give more intensive signals. The samples were heated in opened ceramic pans (diameter 5 mm, height 5 mm). The kinetic parameter – activation energy (E_a) was calculated with Ozawa-Flynn-Wall (OFW) method, using 5 different heating rates. The basic principle of OFW method is that at a constant conversion, the plot lgβ versus 1/T, obtained from a series of experiments performed at several heating rates, results as a straight line whose slope allows evaluation of E_a. The conversion fraction (α) is calculated from the mass change of material during one process. At each temperature α is calculated from mass loss as the difference between initial mass and the mass at exact temperature divided with a difference between initial mass and the mass at the end of the process. E_a is calculated for each value of α individually. In the average, all calculated E_a of oxidation complies with the graphite oxidation activation energy equal to 2.01 eV [6]. The calculated oxidation activation energy for the CFC dust material is 1.99±0.16 eV. In case of sublimation in inert atmosphere (N_2), the process is more affected by particles size; the smaller particles are decomposing and subliming faster than the bigger particles. The activation energy for sublimation of CFC dust material is 1.7±0.6 eV. Furthermore the values of E_a are decreasing while α increase, meaning that sublimation process is affected not only by size of particles but by volume of initial sample as well. From these reasons for using the kinetic parameters, like of E_a oxidation for describing the CFC dust containing materials, a heating in air atmosphere was proposed.

The set of analytical methods was used to characterize the inactive CFC dust material as the reference material for inactive mixtures containing CFC dust and active dust collected form JET vacuum vessel.

Analysis of additives of fullerene C_{60} and long-chain hydrocarbons
Plasma-wall interaction in uncovered places may lead to formation of carbon based compounds like fullerenes and long-chain hydrocarbons. In order to analyse such dust and flakes, pre-analysis of several long-chain hydrocarbons and fullerene C_{60} was performed to use the obtained results for next steps – analysis of mixtures prepared from inactive CFC dust material and chosen additions. Each component was analysed with FT-IR and Raman spectroscopy and with TG/DTA. Three of long-chain hydrocarbons with lowest boiling points - n-Eicosane, n-Triacontane and n-Tetracontane, were analysed with gas chromatography (Shimadzu GC 2010 gas chromatograph). In the chromatogram three separate peaks were observed.

In FT-IR spectra three types of bond are observed for all analysed long chain hydrocarbons. The observed bonds are in agreement with described in literature: CH_2 and CH_3 stretching modes at 2850, 2920, and 2954 cm^{-1}, an HCH scissor at 1474 cm^{-1}, a CH_3 asymmetric bending mode at 1464 cm^{-1}, a methyl symmetric and methylene wagging mode at 1370 cm^{-1}, and a methylene rocking doublet at 719 and 729 cm^{-1}. The advantage for using transmittance FT-IR for analysing mixtures containing long chain-hydrocarbons is the high qualitative sensibility to stretching and bending deformations of C-H bonds. The disadvantage is the fact that signal intensity is more dependent of the amount of C-H bonds overall the sample, not from length of chain. In Raman spectra of long-chain hydrocarbons characteristic signals at frequencies of single bonds to hydrogen and carbons are observed and are in agreement with literature: terminal rocking of methyl group at 835-975 cm^{-1}, -CH_3 in unbranched alkyls at 1056-1060 cm^{-1} and –CH_2- at 1070-1140 cm^{-1}, -

CH$_3$ in unbranched alkyls at 1135-1150 cm^{-1}, -CH$_2$- at 1295-1305 cm^{-1} and –CH$_2$- at 1443-1473 cm^{-1} [9].

In FT-IR spectrum of fullerene C$_{60}$ four allowed modes at 526, 575, 1182 and 1429 cm^{-1} are observed. In Raman spectrum the most intensive signal is at 1425 cm^{-1}, the Raman active modes at 534, 709, 772, 1425, 1575 cm^{-1} are observed as well but with comparable weaker intensities. In p-XRD pattern of C$_{60}$ eight reflexes, in interval from 10 to 35 degree, are observed: 111; 220; 311; 222; 331; 420; 422 and 511. Only a 331 reflex is partially overlapping with graphite 002 reflexes. That shows that it is possible to distinguish the presence of crystalline fullerene C$_{60}$ in graphite containing sample.

The thermal analysis was performed for each separate substance and for mixtures prepared from long-chain hydrocarbons and fullerene C$_{60}$. Separate long-chain hydrocarbons and fullerene C$_{60}$ were heated with two heating rates in air atmosphere to compare the mass change and heat effects, like melting and decomposition heat. With slow heating rate 1 kmin^{-1}, the detection of mass change is more precise. With a faster heating rate 10 Kmin^{-1} the heat effects (changes in DTA signal) are more clearly observable. The melting temperatures of five separately analysed long-chain hydrocarbons were compared with theoretical and given by producer. The values of obtained melting temperatures are summarized in Table 1. Calibration of DTA signal for temperatures and enthalpies was performed using Sn, In, Ag and Au. The temperature accuracy from calibration is ±2 K, melting enthalpy is ±5 kJ.mol^{-1}. Heating separate n-triacontane and n-tetracontane and additional endothermic peak appears just before melting, that could be because of phase changes in structure of these hydrocarbons.

The enthalpies of melting were calculated to obtain if this parameter can be used to quantitate the amount of long-chain hydrocarbons present in CFC dust. Calculated melting enthalpies (Table 4.1) can be used as additional information to determine presence of hydrocarbons in mixtures. However the results are not exactly fitting to theoretical values the combination of obtained melting temperature and calculated enthalpy can be used for detecting presence of long-chain hydrocarbons in mixtures.

Table 4.1
Melting points and enthalpies of separate long-chain hydrocarbons

Compound	Melting point, K		Melting enthalpy, kJ.mol^{-1}	
	Theoretical	Experimental	Theoretical	Experimental
n-Eicosane	310	309	69.9, 204.1	101±48
n-Triacontane	338, 337-338	337	68.3, 167.1	106±18
n-Tetracontane	355, 353-354	351	135.5	141±76
Pentacontane	365, 365-366	363	162.4	265±41
Hexacontane	372, 371-372	369	193.2	166±10

For further investigations it was assumed that dust collected from JET vacuum vessel contain basically carbon and additions of hydrocarbons.

There were made mixtures with addition of separate long chain hydrocarbons. The mixtures were made by adding one or several long-chain hydrocarbons to CFC. One set of mixtures was made in such way that to 95 mg of CFC was added 5 mg of either one of hydrocarbons or fullerene C$_{60}$. For precise observation of mass change slow heating rate 1 Kmin^{-1} was used. It was obtained that in mixture containing CFC dust materials and an addition, until decomposition of additive practically no mass change can be observed. As the decomposition of additives is exothermic, it enhances decomposition of CFC dust particles as well. A slight slope in mass change of CFC appears just after decomposition of additive, consequently presence of long-chain hydrocarbons and fullerene C$_{60}$ enhances

decomposition of CFC dust material. Thus it was concluded that the heating rate can be increased to obtain the heat effects, but not too much to still obtain the mass exchanges.

Mixtures containing exact amount of long chain-hydrocarbons were heated in nitrogen atmosphere with heating rate 10 $Kmin^{-1}$. The complete decomposition of additives took place with sharp decrease of ass at decomposition temperature, but the DTA signals were less intensive. Heating a mixture of long-chain hydrocarbons in same conditions, several endothermic peaks were observed, but because of overlapping, it was not possible to distinguish precisely each hydrocarbon form its melting temperature. Mixing together long chain hydrocarbons and heating them in air, the same tendency appear – the melting temperatures are overlapping.

As an optimum for thermal analysis of mixtures containing comparably small (≤2%) amount of long-chain hydrocarbons and fullerene C_{60}, a heating rate 5 $Kmin^{-1}$ was preferred, optimal mass of analysed sample was found to be around 5 mg. In this case it is possible to distinguish the melting processes between separate additives.

Analysis of deposited and collected carbon dust

Dust collected from JET vacuum vessel in 2010 "Pot D" were analysed with SEM and EDX. The particle size is comparable with dust material prepared from inactive CFC tile. Particle size varies from nanometre-size to several hundred μm. From the shape particles can be separated in flakes, layered pieces, particles with irregular shape, with smooth, layered or porous surface. The groups can be generalized in two main groups: flakes – particles that exhibit a layered structure, representing the archaeological deposition and dust – particles with globular or irregular shape. Size of flakes can be up to 0.5 mm, thickness is mostly several tens of μm. Surface of flakes is either smooth or with cracks. The cross-section of flakes represents several with several distinguishable layers. Dust particles with size around 10-50 μm contain impurities – oxygen, nickel, boron, chromium, beryllium. From Raman spectra it is obtained that dust and flakes contain graphite (a G-peak at 1585 cm^{-1}) and disordered graphite structures (D-peak at 1350 cm^{-1}). The broadening of G-peak and intensity ratio I_D/I_G value close to 1 points to presence of amorphous carbon. In other type of Raman spectra photoluminescence background is observed. Increasing photoluminescence background in visible Raman spectrum is a typical signature of increased H content. The sp2 and sp3 hybridized carbon clusters contain different structural units with C=C double bonds and C–H chains, which induce different energy states in band tail and form different radiative recombination centres. Nevertheless in Raman spectrum increasing luminescence level and graphite peaks dominate over other signals, a shoulder in spectrum observed around 840 cm^{-1} might correspond to terminal rocking of methyl group at 835-975 cm^{-1}. In Raman spectrum of deposited layer on side surface of inner divertor vertical tile No.3 the luminescence background is even dominating over the graphite signals (D- and G-peak). Leading to a conclusion that in dust and flakes collected from JET vacuum vessel contain graphite and hydrogenated carbon particles, but a deposited layer on surface of divertor tile could be hydrogenated amorphous carbon film. Surface of deposited layer is rough, contains bubble-like structures and is light reflecting, showing that it might contain metallic impurities.

The structure of CFC tile was investigated also in direction from plasma facing surface to bulk of material. Making mapping starting from 5 μm to 65 μm from plasma facing surface, no periodical change in shape of spectra is observed. The characteristic parameter, intensity ratio between D- and G-peak varies from 0.2-0.5. That allows concluding that formation of amorphous hydrogenated carbon films forms more intensively on the surface of divertor tiles and already in few micrometres in bulk of CFC material, spectra of graphite material are close to reference.

On tungsten covered surfaces, in places where due to plasma wall interaction, the tungsten layer has been ablated, presence of tungsten oxide is observed. In Raman spectrum it appears as a broad, intensive signal at around 800 cm^{-1}.Tungsten oxide may form in temperatures above 800 K.

Although the main changes in structure and content takes place on plasma facing surface, the presence of hydrogen containing compounds in bulk of material is observed. Thermal desorption spectroscopy show that in lower temperatures substances with small mass (2, 4) are released. Higher masses (12-18) are released in higher temperatures, over 1300 K, with heating rate 4 Ks^{-1}.

4.3. Tritium release from beryllium pebbles of HIDOBE-01 experiment on annealing under action of electron radiation and magnetic field

Principal investigator: G. Kizane
A. Vītiņš, A. Matīss, G. Ivanov, V. Kinerte, J. Jansons

Beryllium pebbles are foreseen as a neutron multiplier to ensure sufficient tritium breeding in a ceramic breeder in the European Helium-Cooled Pebble-Bed (HCPB) breeding blanket for a future demonstration fusion power reactor (DEMO). The 1 mm Be pebbles produced by Rotating Electrode Process (REP) are at present the reference multiplier material for the HCPB breeding blanket and will be used in the first HCPB Test Blanket Modules (TBMs). In the HCPB, the beryllium pebbles will be operated at 573-923 K under intense fast neutron radiation of about 10^{18} n m^{-2} s^{-1} and a high magnetic field of 7-10 T. According to estimations of the present European HCPB concept, in a 40000 h operating time, the beryllium pebbles will receive the neutron fluency up to 3×10^{26} n m^{-2} ($E_n > 1$ MeV), which will produce the displacement damage of about 80 dpa, 25700 appm helium and 640 appm tritium in beryllium.

In the frame of the European programme for the development of the HCPB, a high dose irradiation of beryllium (HIDOBE) was performed in the High Flux Reactor at Petten.
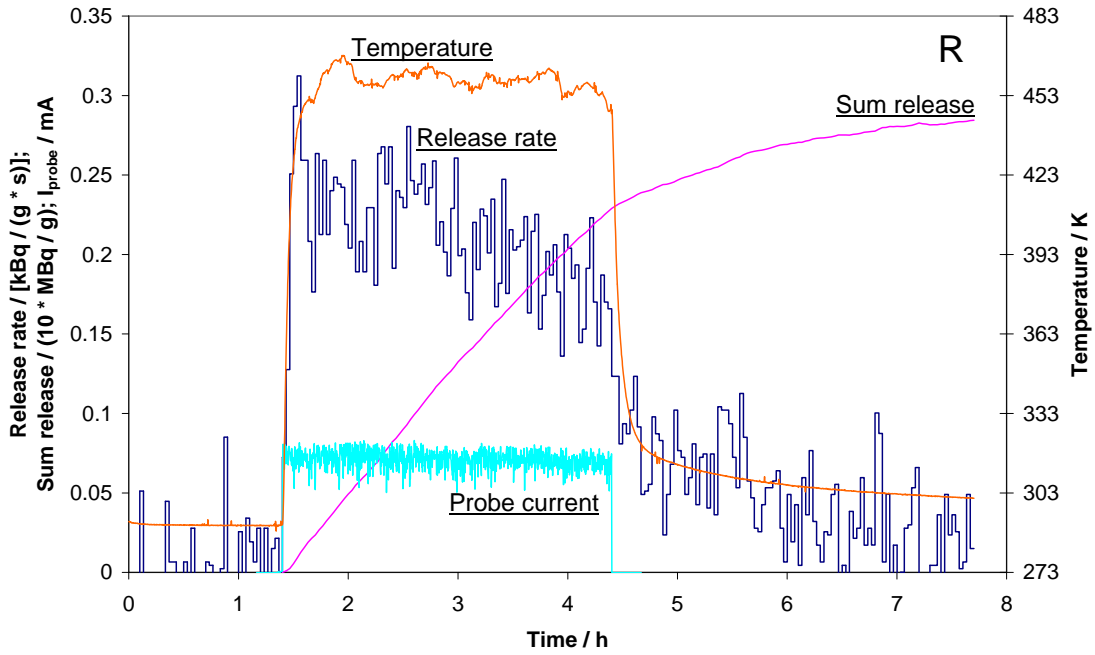
The post-neutron-irradiation experiments in the year 2013 are continuation of tritium release investigations of HIDOBE-01 experiment beryllium pebbles. There were carried out experiments to assess effects of temperature 470-1080 K, 5 MeV fast electron radiation of the dose rate of 10-13 MGy/h and a magnetic field of 1.5-1.7 T on tritium release.

Tritium release from the pebbles of a diameter 0.5 mm and the pebbles of a diameter 1.0 mm, labelled with the year of production 2001 were investigated. The radiation thermomagnetic set up on basis of the electron accelerator in Salaspils was used for investigation of effects of electron radiation and magnetic field on tritium release from pre-irradiated samples. Neutron-irradiated beryllium pebbles were annealed at temperatures up to 1083 K in a continuous flow of He + 0.1% H$_2$ purge gas, enabling exposure to 5 MeV fast electrons of 10-18 MGy/h and a magnetic field of 1.5-1.7 T.
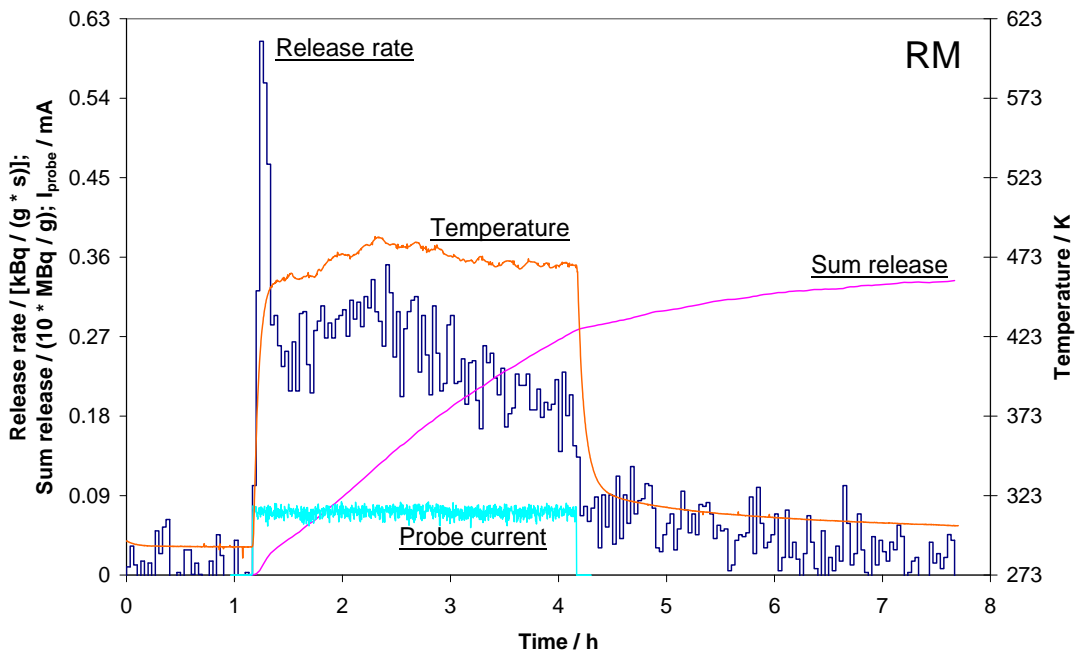
One beryllium pebble was annealed in each tritium release experiment. The tritium release experiments and data acquisition were realized analogous to the experiments as in the previous years. Experiment series of irradiations with 5 MeV fast electrons were planned for this study with successively increasing temperatures of the Be pebble under study-480 (without additional heating), 780, 830, 880, 930, 978, 1045 and 1078 K. Pairs of experiments of each type were performed – one without magnetic field and another one with a magnetic field of 1.5-1.7 T.

Results of tritium release experiments with a pair of 1.0 mm pebbles
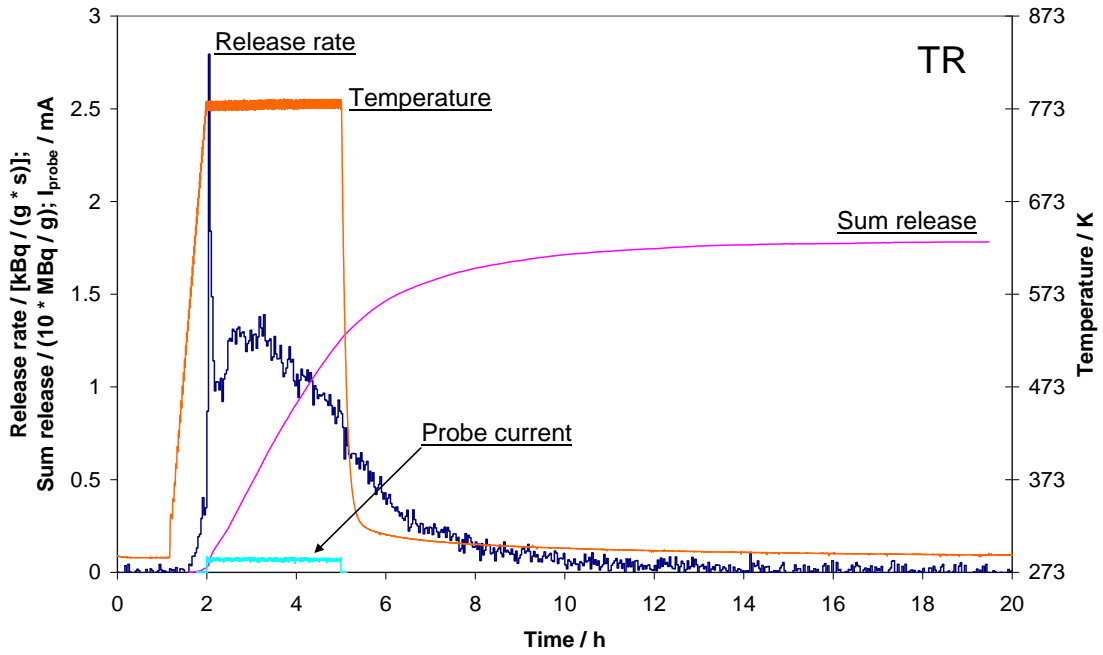Tritium release curves of the series of post neutron-irradiation experiments with a pair of the 1.0 mm pebbles labelled with the year of production 2001 (pebbles code 46sPC/3/08 and 46sPC/3/09) are shown in Figs.4.3.1 -4.3.16. The acting factors in figures are denoted as T – temperature as a result of external heating under the given temperature program, R – 5 MeV fast electron radiation of the dose rate 10-13 MGy/h, M – a magnetic field of 1.5-1.7 T.
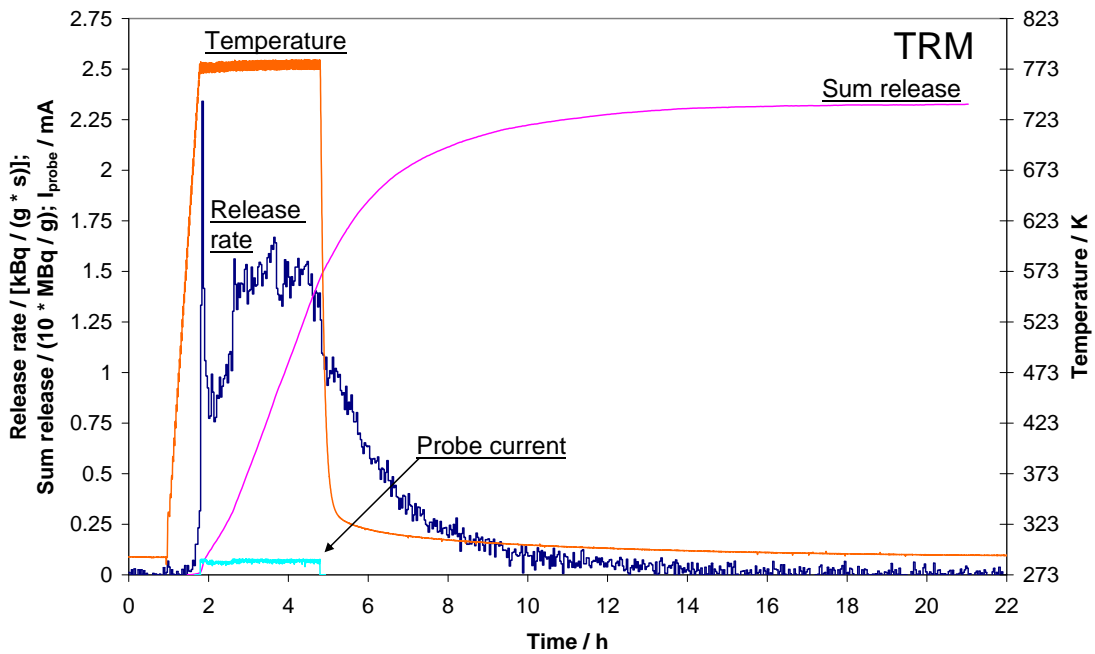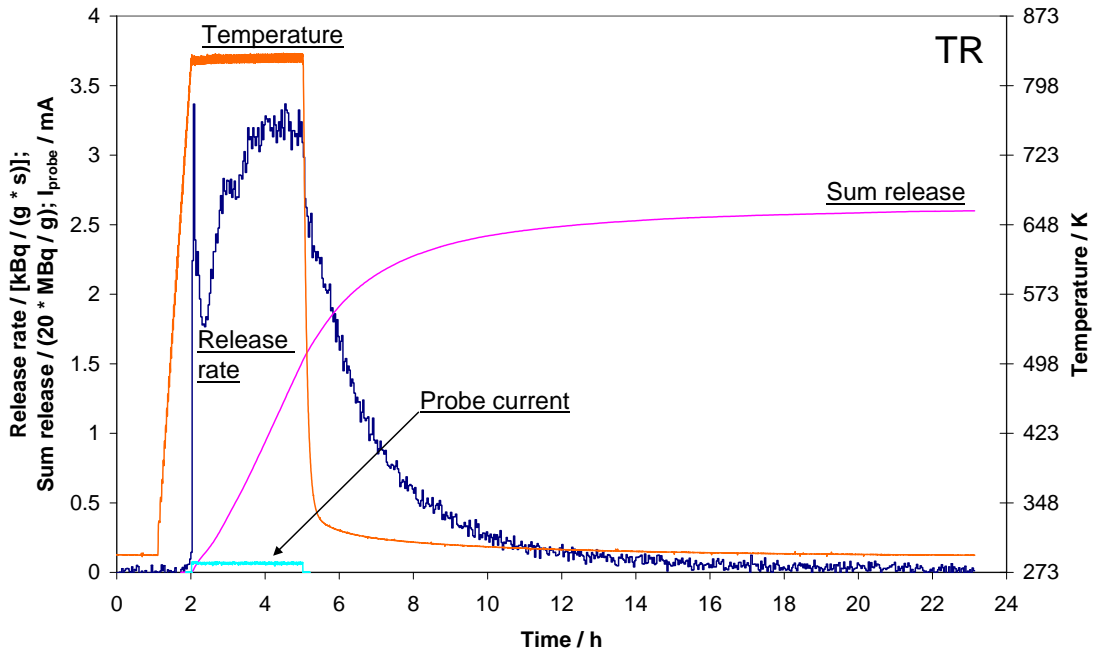
Fig.4.3.1. Tritium release from pebble 46sPC/3/08. The maximum temperature: 468 K. The estimated dose of the electron irradiation: 37.3 MGy (the average electron flux 1.097×10^{13} electrons cm^{-2} s^{-1}). The final tritium sum release: 2.85 MBq/g (0.015% of the estimated initial total tritium 19.2 GBq/g).

Fig. 4.3.2. Tritium release from pebble 46sPC/3/09. The maximum temperature: 486 K. The estimated dose of the electron irradiation: 37.5 MGy (the average electron flux 1.104×10^{13} electrons cm^{-2} s^{-1}). The final tritium sum release: 3.33 MBq/g (0.017% of the estimated initial total tritium 19.2 GBq/g).
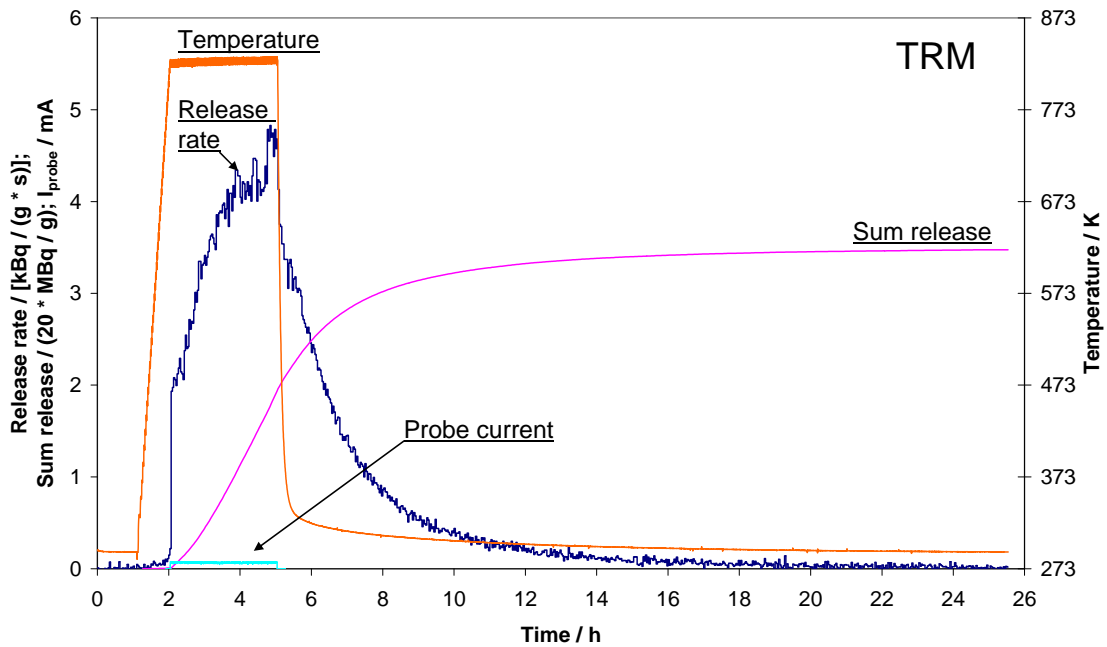
Fig. 4.3.3. Tritium release from pebble 46sPC/3/08. The maximum temperature: 784 K. The estimated dose of the electron irradiation 36.4 MGy (the average electron flux 1.072×10^{13} electrons cm^{-2} s^{-1}). The final tritium sum release: 17.8 MBq/g (0.093% of the estimated initial total tritium 19.2 GBq/g).
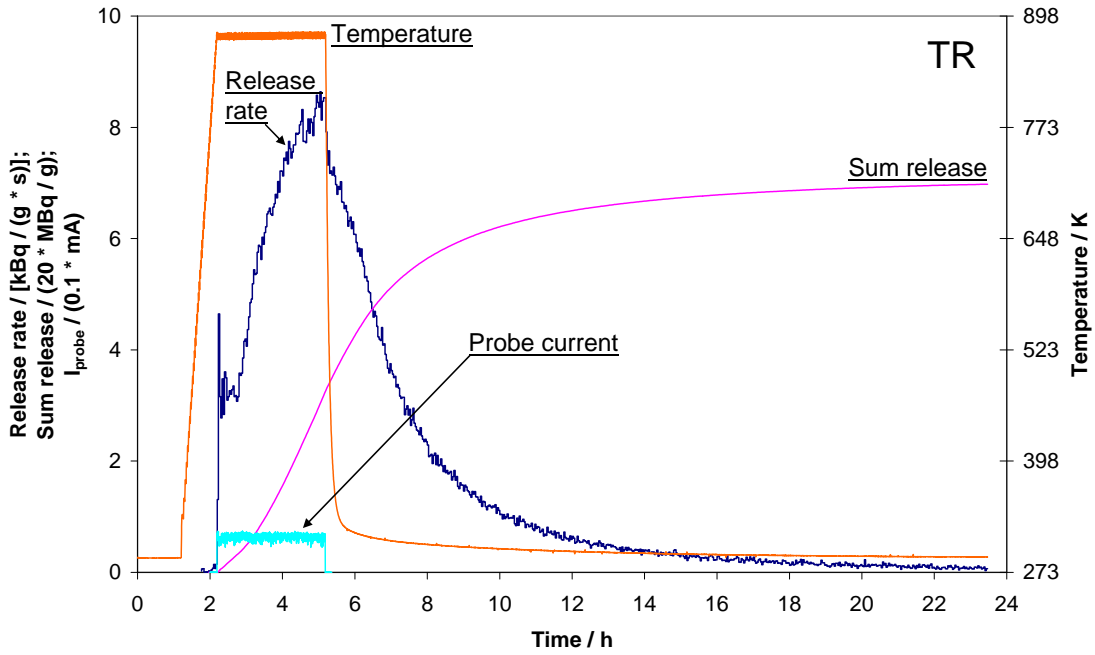

Fig. 4.3.4. Tritium release from pebble 46sPC/3/09. The maximum temperature: 782 K. The estimated dose of the electron irradiation: 35.2 MGy (the average electron flux 1.036×10^{13} electrons cm^{-2} s^{-1}). The final tritium sum release: 23.3 MBq/g (0.12% of the estimated initial total tritium 19.2 GBq/g).
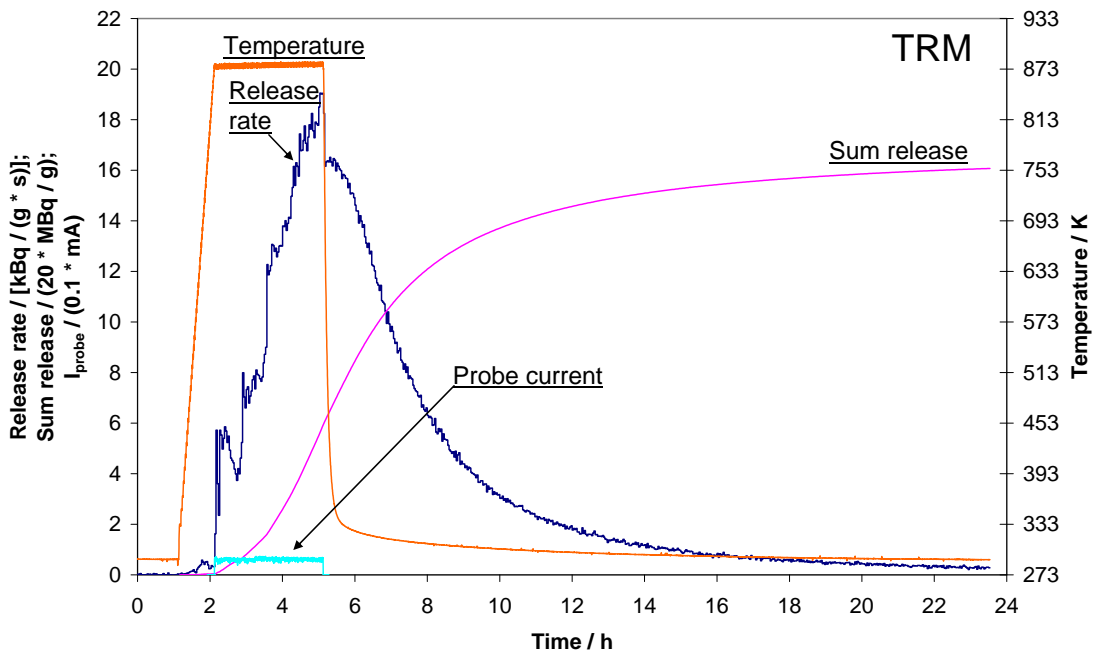
Fig. 4.3.5. Tritium release from pebble 46sPC/3/08. The maximum temperature: 833 K. The estimated dose of the electron irradiation: 34.9 MGy (the average electron flux 1.027×10^{13} electrons cm^{-2} s^{-1}). The final tritium sum release: 52.0 MBq/g (0.27% of the estimated initial total tritium 19.2 GBq/g).
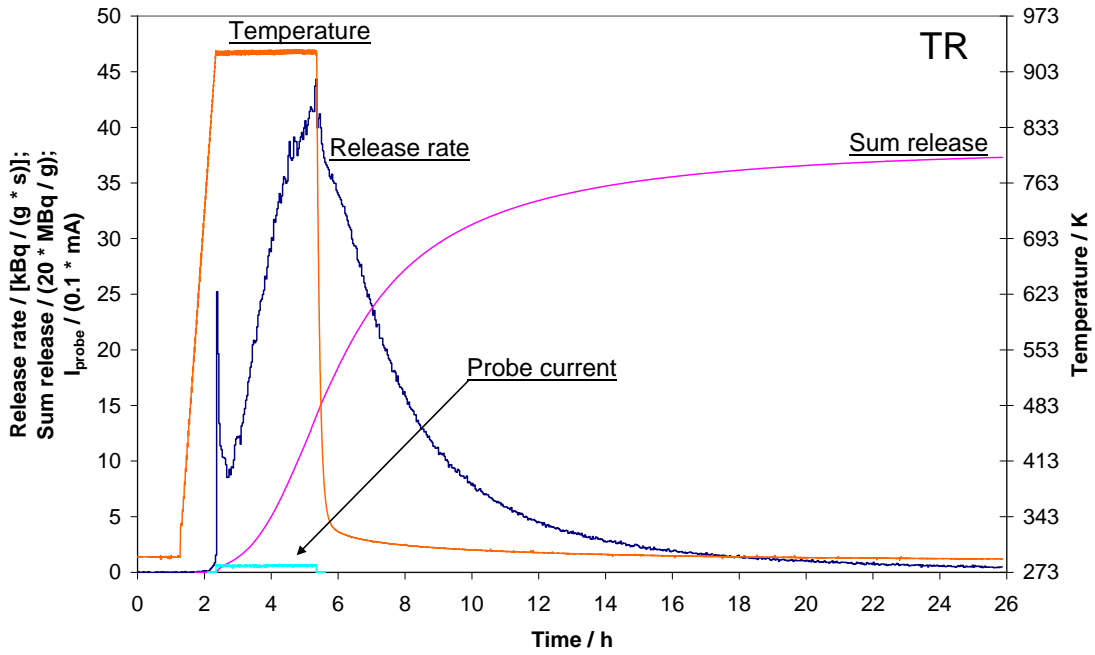

Fig. 4.3.6. Tritium release from pebble 46sPC/3/09. The maximum temperature: 831 K. The estimated dose of the electron irradiation: 35.5 MGy (the average electron flux 1.046×10^{13} electrons cm^{-2} s^{-1}). The final tritium sum release: 69.5 MBq/g (0.36% of the estimated initial total tritium 19.2 GBq/g).

Fig. 4.3.7. Tritium release from pebble 46sPC/3/08. The maximum temperature: 880 K. The estimated dose of the electron irradiation: 33.3 MGy (the average electron flux 0.980×10^{13} electrons cm^{-2} s^{-1}). The final tritium sum release: 140 MBq/g (0.73% of the estimated initial total tritium 19.2 GBq/g).
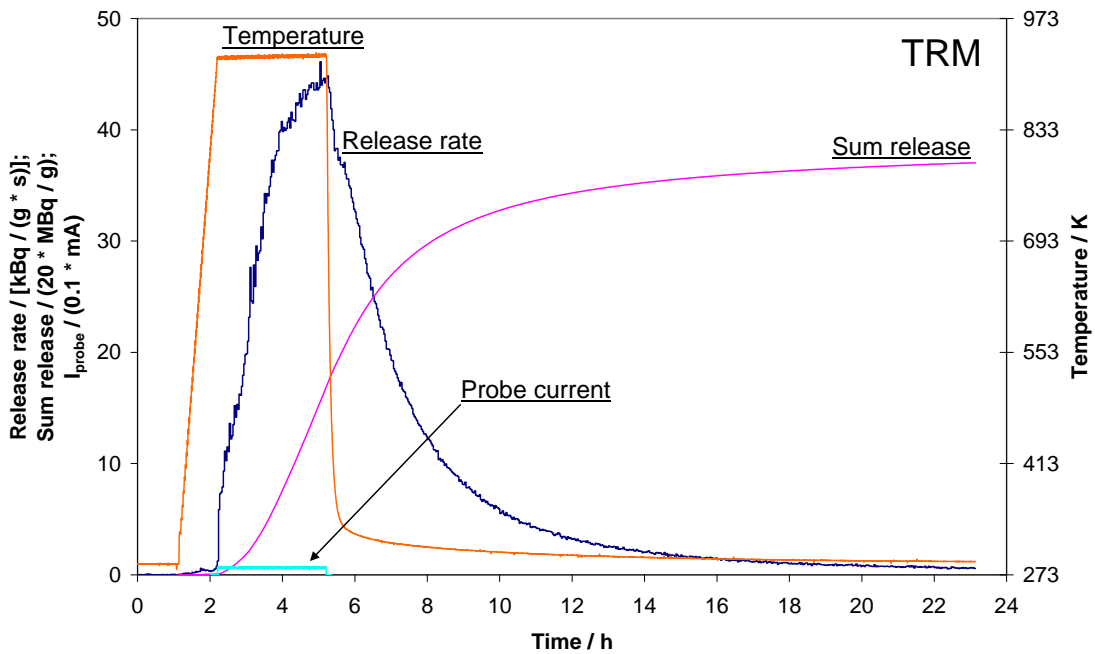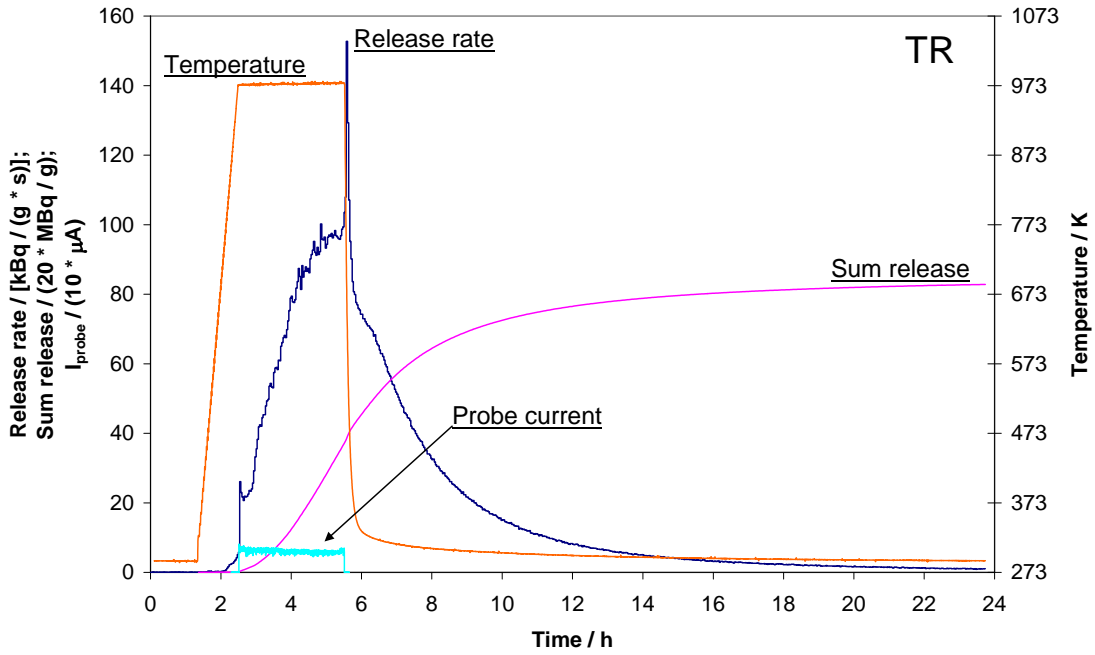

Fig. 4.3.8. Tritium release from pebble 46sPC/3/09. The maximum temperature: 882 K. The estimated dose of the electron irradiation: 31.9 MGy (the average electron flux 0.940×10^{13} electrons cm^{-2} s^{-1}). The final tritium sum release: 321 MBq/g (1.67% of the estimated initial total tritium 19.2 GBq/g).

Fig. 4.3.9. Tritium release from pebble 46sPC/3/08. The maximum temperature: 930 K. The estimated dose of the electron irradiation: 31.6 MGy (the average electron flux 0.930 × 10^{13} electrons cm^{-2} s^{-1}). The final tritium sum release: 746 MBq/g (3.89% of the estimated initial total tritium 19.2 GBq/g).
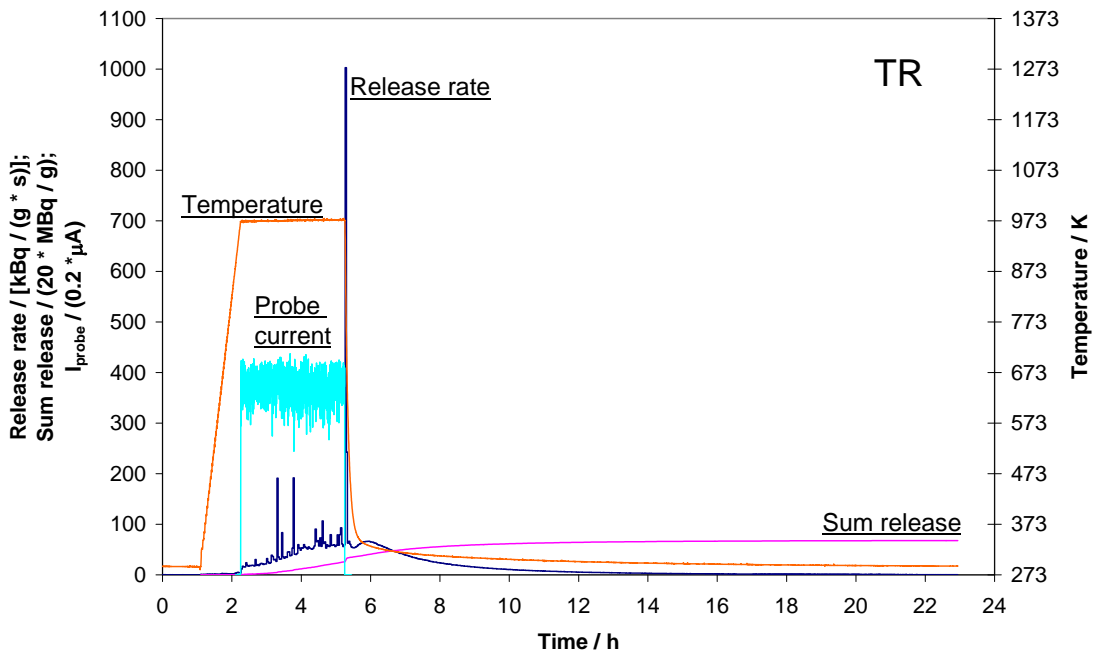

Fig. 4.3.10. Tritium release from pebble 46sPC/3/09. The maximum temperature: 930 K. The estimated dose of the electron irradiation: 33.8 MGy (the average electron flux 0.995 × 10^{13} electrons cm^{-2} s^{-1}). The final tritium sum release: 741 MBq/g (3.86% of the estimated initial total tritium 19.2 GBq/g).

Fig. $.3.11. Tritium release from pebble 46sPC/3/08. The maximum temperature: 979 K. The estimated dose of the electron irradiation: 31.8 MGy (the average electron flux 0.936 × 10^{13} electrons cm^{-2} s^{-1}). The final tritium sum release: 1.66 GBq/g (8.63% of the estimated initial total tritium 19.2 GBq/g).
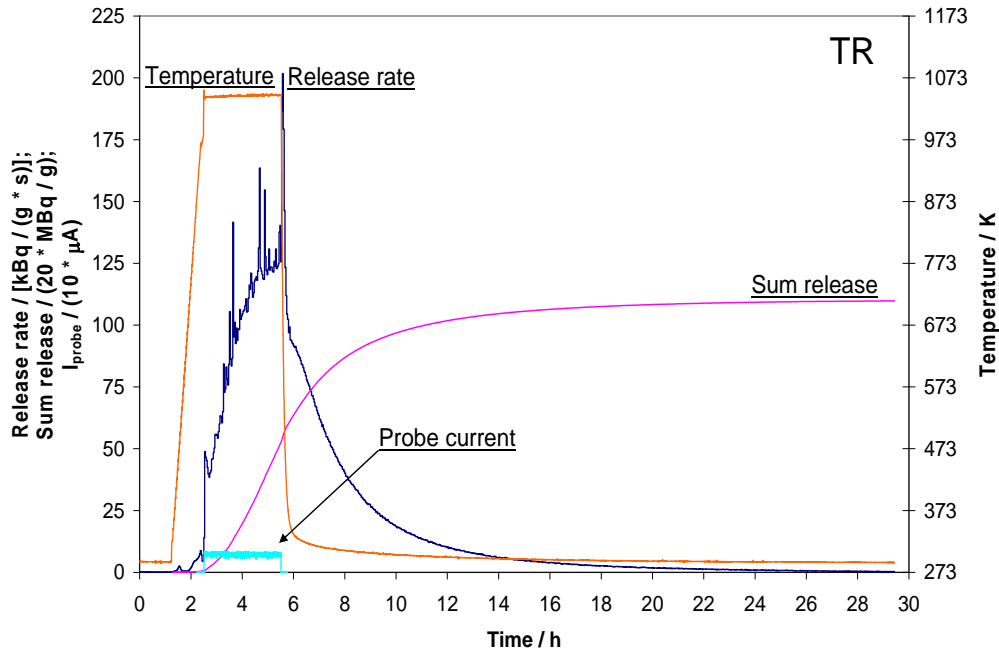

Fig. 4.3.12. Tritium release from pebble 46sPC/3/09. The maximum temperature: 978 K. The estimated dose of the electron irradiation: 39.3 MGy (the average electron flux 1.156 × 10^{13} electrons cm^{-2} s^{-1}). The final tritium sum release: 1.35 GBq/g (7.05% of the estimated initial total tritium 19.2 GBq/g).

Fig. 4.3.13. Tritium release from pebble 46sPC/3/08. The maximum temperature: 1053 K. The estimated dose of the electron irradiation: 38.6 MGy (the average electron flux 1.135 × 10^{13} electrons cm^{-2} s^{-1}). The final tritium sum release: 2.20 GBq/g (11.5% of the estimated initial total tritium 19.2 GBq/g).
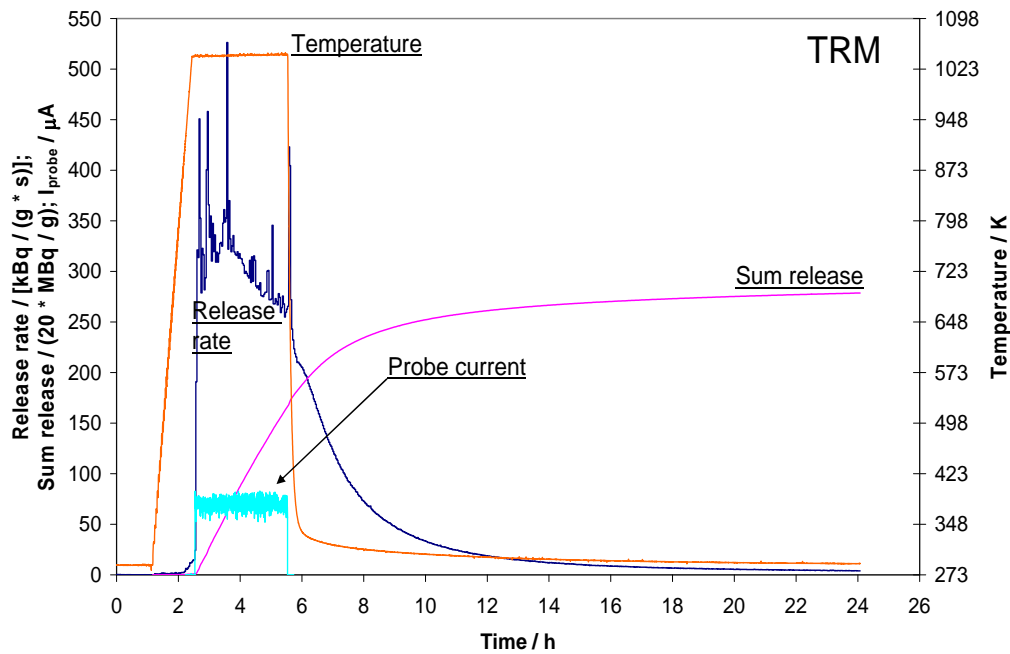

Fig. 4.3.14. Tritium release from pebble 46sPC/3/09. The maximum temperature: 1047 K. The estimated dose of the electron irradiation: 37.1 MGy (the average electron flux 1.093 × 10^{13} electrons cm^{-2} s^{-1}). The final tritium sum release: 5.57 GBq/g (29.0% of the estimated initial total tritium 19.2 GBq/g).
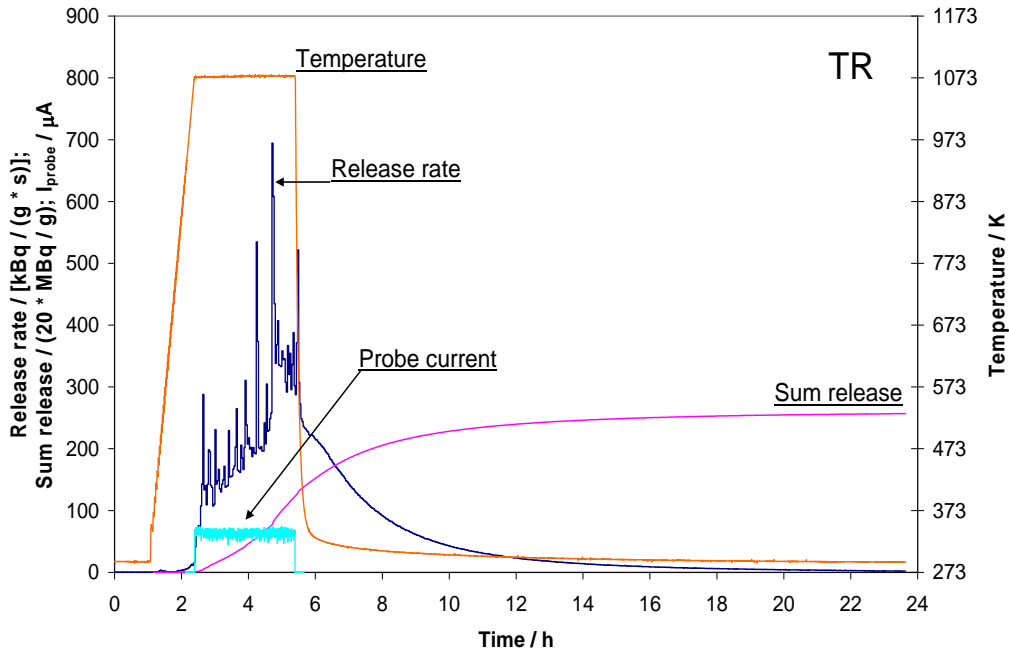
Fig. 4.3.15. Tritium release from pebble 46sPC/3/08. The maximum temperature: 1078 K. The estimated dose of the electron irradiation: 33.6 MGy (the average electron flux 0.990×10^{13} electrons cm^{-2} s^{-1}). The final tritium sum release: 5.14 GBq/g (26.8% of the estimated initial total tritium 19.2 GBq/g).
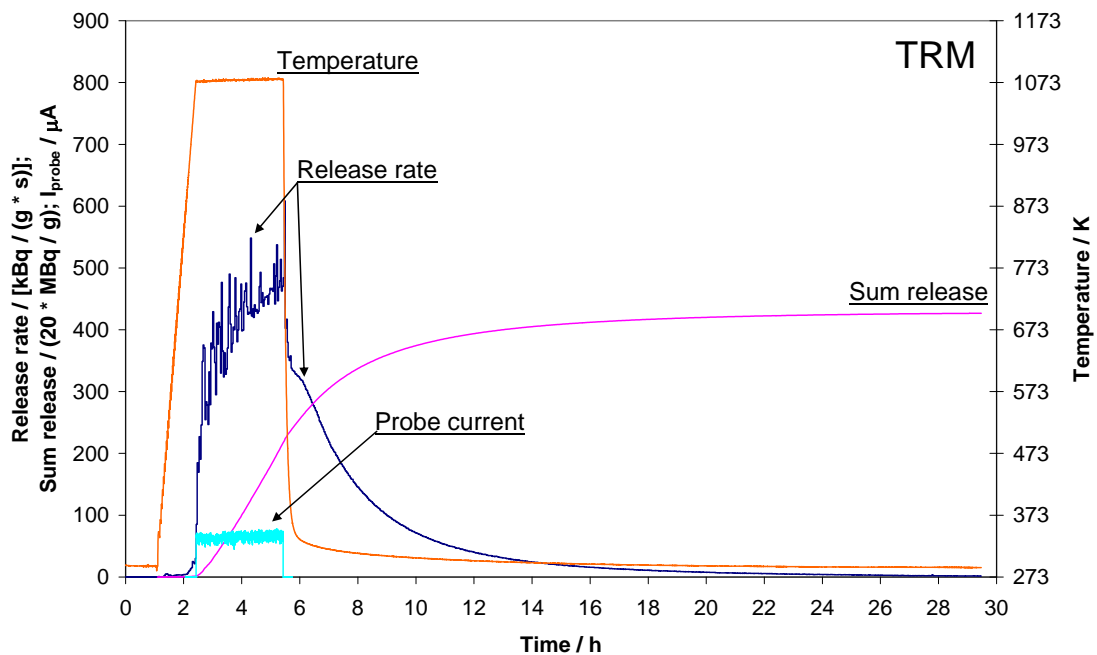

Fig. 4.3.16. Tritium release from pebble 46sPC/3/09. The maximum temperature: 1081 K. The estimated dose of the electron irradiation: 34.2 MGy (the average electron flux 1.007×10^{13} electrons cm^{-2} s^{-1}). The final tritium sum release: 8.53 GBq/g (44.4% of the estimated initial total tritium 19.2 GBq/g).

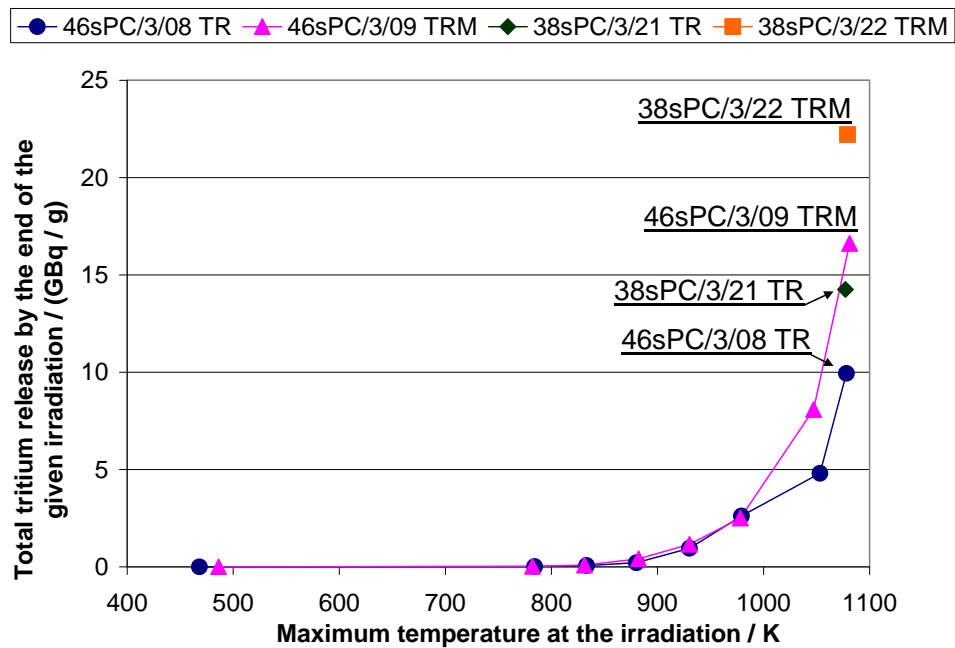The tritium release rate in all the experiments of the series was not uniform. Most of the curves of the tritium release rate have a sharp maximum shortly after switching on the 5 MeV electron radiation. A sharp maximum is also present in all the curves of the tritium

release rate on switching off the electron radiation and the temperature program in the temperature range 978-1081 K (Figs. 4.3.11-4.3.16). Sharp maximums of the tritium release rate occurred also during the electron irradiation with the external temperature program of 1047-1081 K (Figs. 4.3.12-4.3.16). Sharp maximums of the tritium release rate are indicative of the tritium burst release; however they had no large contribution in the final tritium sum release.

A common feature of most of the curves of the tritium release rate is a general ascending trend with time during the electron irradiation with the external temperature program of a constant temperature in a range of 831-1081 K (Figs. 4.3.5-4.3.16). The ascending trend of the tritium release rate indicates about activation of the tritium release under the given conditions of experiments. The activation is also evident from the fact that a considerable fraction of the final tritium sum release – up to 60% (Fig. 4.3.15) is released from a cooling pebble during 15 h after switching off the electron radiation and the temperature program. This type of activation of tritium release results in the fact that the time required for one experiment is about 24 h. As a practical significance of the activation of the tritium release, it is clearly visible from the curves of the tritium release rate (Figs. 54.3.5-4.3.16) that prolongation of the electron irradiation with the external temperature program 831-1081 K should considerably increase the degree of detritiation of the pebble under study.

Fig. 4.3.17 Cumulative activity of the tritium released in successive anneals with electron irradiation for 3 h with increasing temperature without magnetic field (pebble 46sPC/3/08) and in a magnetic field of 1.5-1.7 T (pebble 46sPC/3/09) as a function of the maximum temperature in the given anneal. Values of the tritium cumulative release from pebbles 38sPC/3/21 and 38sPC/3/22 (Figs. 4.3.18 and 5.3.19, respectively) are given for comparison.

The curves of the total tritium release in Fig. 4.3.17 for pebbles 46sPC/3/08 and 46sPC/3/09 have been obtained by summing the values of the final tritium sum release in successive electron irradiation experiments with increasing temperature shown in Figs. 5.3.11-5.3.16. Up to 873 K the tritium release was little in comparison to the total amount of tritium in the pebbles estimated to be 19.2 GBq/g. Tritium release rate significantly increased above 873 K. The curves of the total tritium release of pair of pebbles with ∅ 1 mm 46sPC/3/08-46sPC/3/09 (Fig. 4.3.17) indicate a possible appreciable facilitating effect

of a magnetic field of 1.5-1.7 T at temperatures above 973 K as by about 60% larger tritium release at 1040-1081 K.

Results of tritium release experiments with a pair of 0.5 mm pebbles

Only one post neutron-irradiation tritium release experiment at 1070-1079 K was performed with each pebble of pair 38sPC/3/21-38sPC/3/22. Their results are shown in Figs. 4.3.18 and 4.3.19 respectively. A sharp tritium release peak occurred on switching on the electron radiation. During the electron irradiation, the tritium release rate was not uniform; its curves have minor peaks. Also in the case of the 0.5 mm pebbles, the activation of the tritium release at temperatures 1070-1079 K is visible from the curves of the tritium release rate, and about 45% of the final tritium sum release was released from a cooling pebble during 15 h after switching off the electron radiation and the external temperature program. It is visible from the curves of the tritium release rate (Figs. $.3.18 and 4.3.19) that prolongation of the electron irradiation with the external temperature program 1070-1079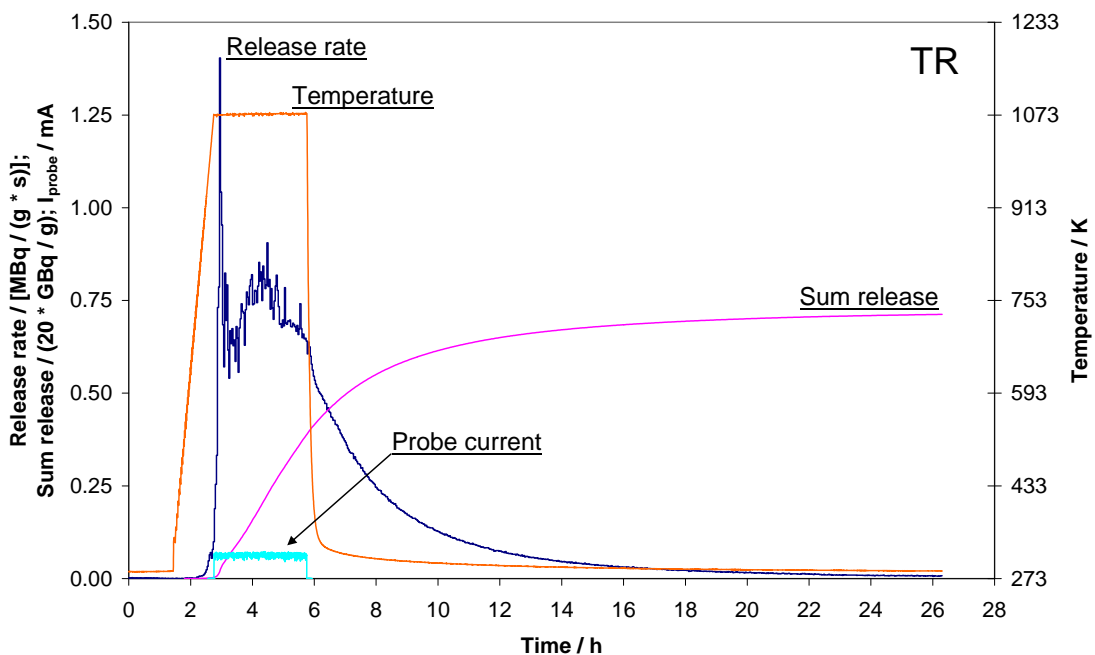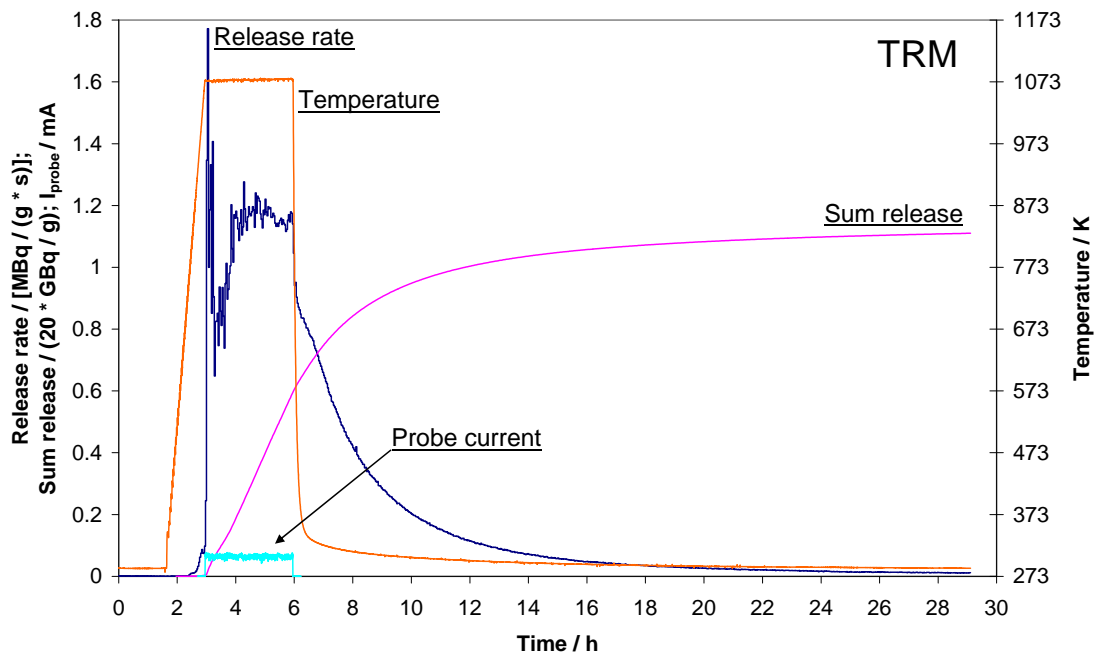 K could increase the degree of detritiation of the pebbles. The comparison of the values of the tritium sum release of pebble pair 38sPC/3/21-38sPC/3/22 indicates a possible facilitating effect of a magnetic field of 1.5-1.7 T on the final tritium sum release by 56%.

Fig. 4.3.18. Tritium release from pebble 38sPC/3/21 (798 K), m=0.18 mg, $\varnothing$0.54 mm. The maximum temperature 1077 K; without magnetic field; an electron irradiation for 3 h with the estimated dose 33.1 MGy (the average electron flux 0.973×10^{13} electrons cm^{-2} s^{-1}). The final tritium sum release: 14.25 GBq/g (74.2% of the estimated initial total tritium 19.2 GBq/g).

Fig. 4.3.19 Tritium release from pebble 38sPC/3/22 (798 K), m=0.16 mg, ⌀0.53 mm. The maximum temperature 1079 K; in a magnetic field of 1.5-1.7 T; an electron irradiation for 3 h with the estimated dose 34.0 MGy (the average electron flux 1.000×10^{13} electrons $cm^{-2} s^{-1}$). The final tritium sum release: 22.21 GBq/g (116% of the estimated initial total tritium 19.2 GBq/g).

The ascending trend of the curves of the tritium release rate on annealing at a constant temperature with simultaneous 5 MeV electron radiation (Figs. 4.3.5 - 4.3.16) indicates that the electron radiation produces structural changes in the neutron-irradiated Be pebble that facilitate tritium release. For comparison, descending curves of the tritium release rate at a constant temperature correspond to the tritium release controlled by atomic diffusion Annealing of the pebbles under temperature programmes similar to those in Figs. 4.3.5 - 4.3.16 without electron radiation should determine the possible stimulating contribution of the electron radiation in the tritium release.

Most of the tritium (about 90%) in the 0.5 and 1.0 mm pebbles irradiated with neutrons in the HIDOBE temperature zones 798 and 923 K previously is determinate to be molecular tritium, which is apparently localized in the helium bubbles in the pebbles. The 5 MeV electron radiation possibly produces microcrevices in the pebble, which facilitates tritium release during the annealing with the electron radiation and enables a following appreciable tritium release from a cooling pebble. Opening of the tritium-containing helium bubbles to the outer surface of the pebble may be a reason of the sharp tritium burst release peaks in the tritium release curves in the present study.

The results of the post neutron-irradiation tritium release experiments in the year 2013 indicate a facilitating effect of a magnetic field of 1.5-1.7 T with the simultaneous 5 MeV fast electron radiation at temperatures above 1040 K on the tritium release, but because of the fact that only one pair of pebbles was investigated on the magnetic field effect from each batch, the ability to draw general quantitative conclusions about the magnetic field effect is very limited by possible dissimilarity of the pebbles within the batch with respect to their initial total tritium amount and their tritium release properties.

Summarizing results show that the tritium release rate on annealing of HIDOBE-01 798 K neutron-irradiated beryllium pebbles with simultaneous 5 MeV fast electron radiation was not uniform – it had strong irregular oscillations particularly in the case of 1.0 mm pebbles.

The sharp peaks of the release rate were indicative of burst release, which is characteristic to opening of tritium-containing gas inclusions. The distinctive ascending trend of the tritium release rate on annealing at a constant temperature 830-1081 K with simultaneous 5 MeV fast electron radiation and a considerable following released fraction from a cooling pebble after the end of the annealing are indicative of activation of the tritium release by the electron radiation – possibly by production of structural changes, e.g. microcrevices, in the neutron-irradiated Be pebbles that facilitate the tritium release. The ascending curves of the tritium release rate at a constant temperature correspond to a release process that is different from the release determined by atomic diffusion, which is characterized by a descending tritium release rate at a constant temperature. Up to 873 K the tritium release of the HIDOBE-01 798 K Be pebbles was less than 3% with respect to the total amount of tritium in the pebbles estimated to be 19.2 GBq/g. Tritium release rate significantly increased above 873 K. This phenomenon is in line with the fact that a considerable in-pile tritium release took place during the HIDOBE-01 neutron irradiation only from the beryllium pebbles at 923 K and 1023 K rather than from the pebbles at 698 K and 798 K. A considerable facilitating effect (56-67%) of a magnetic field of 1.5-1.7 T with the simultaneous 5 MeV fast electron radiation on the tritium release from the HIDOBE-01 798 K 1.0 and 0.5 mm Be pebbles on annealing at temperatures above 1040 K was observed, but because of the fact that only one pair of pebbles was investigated on the magnetic field effect from each batch, the ability to draw general quantitative conclusions about the magnetic field effect is very limited by possible dissimilarity of the pebbles within the batch with respect to their initial total tritium amount and their tritium release properties.

4.4. Development of advanced ceramic breeder materials having improved structure and radiation stability

Principal investigator: **G.Kizane**
A. Zarins, L. Baumane, Br. Lescinskis, O. Valtenbergs, A. Supe

The helium-cooled pebble bed (HCPB) is one of the concepts developed in Europe for the breeding blanket of the future DEMO/Power Plant. In the HCPB blanket, beryllium or beryllide pebbles ($\varnothing \approx 1$ mm) are planned as a neutron multiplier and Li_4SiO_4 or Li_2TiO_3 ceramic pebbles ($\varnothing \approx 0.4\text{-}0.6$ mm) as a tritium breeder.

In ITER several concepts of Test Blanket Modules (TBMs) will be tested and verified, because the tritium breeding is a key issue in future fusion devices, like DEMO. The HCPB TBM, proposed by the European Union, will use lithium orthosilicate (Li_4SiO_4) pebbles with 2.5 wt.% excess of silica (SiO_2) as reference tritium breeding ceramic.

However, the latest irradiation experiments showed that the reference Li_4SiO_4 pebbles may crack and form fragments under operation conditions as expected in the HCPB TBM. Therefore it has been suggested to change the chemical composition of the reference Li_4SiO_4 pebbles and to replace the excess of SiO_2 by titania (TiO_2).

The goal of the task is investigation a role of the high-temperature radiolysis of Li_4SiO_4 pebbles with additions of Li_2TiO_3 in the frame of WP 2013, the task was realized in cooperation with association EURATOM Germany, KIT.

From previous studies, it is known that the formation, localisation and annihilation of radiation-induced defects (RD) and radiolysis products (RP) will induce changes of thermal and mechanical properties, swelling and degradation of mechanical integrity, and may also affect tritium diffusion and release processes. Most crucial are electron type RD and RP, i.e. E' centres ($\equiv Si\cdot$) and colloidal lithium (Li_n), which can interact with tritium and, due to the high thermal stability of $\equiv Si\text{-}T$ and $Li\text{-}T$ bonds, may cause tritium accumulation. Previously it has been reported that up to 70 % of RD and RP localise in a 50 μm subsurface layer of the reference pebbles, due to intrinsic structural defects.

The modified Li_4SiO_4 pebbles with 10-30 mol% Li_2TiO_3 (screened to 0.65-0.90 mm) were selected for investigation in comparison to the reference pebbles. The high-temperature radiolysis was performed with accelerated electrons by a linear electron accelerator ELU-4 (E=5 MeV) up to 5 GGy absorbed dose at 380-670 K in dry argon. The formation of RD and RP was analyzed by electron spin resonance (ESR) and the phase transitions by powder X-ray diffractometry (p-XRD) and Fourier transform infrared (FT-IR) spectroscopy.

Microstructural changes and phase transitions in modified Li_4SiO_4 pebbles with additions of TiO_2.

The modified Li_4SiO_4 pebbles with different content of TiO_2 before irradiation have two main phases – a primary phase, Li_4SiO_4, and a secondary phase, Li_2TiO_3. The minor metallic impurities, mostly platinum (Pt), within the modified pebbles were detected by qualitative XRF analysis. Under action of accelerated electrons up to 5 GGy absorbed dose at 380-670 K in dry argon atmosphere rapid colour change to the modified and reference Li_4SiO_4 pebbles were observed.

The observed colour changes of the reference and modified Li_4SiO_4 pebbles after irradiation could be attributed to the formation and accumulation of simple and multi-electron centres. Simple electron centres consist of F^+ and F° centres (localized one or two electrons in oxygen vacancies) and E' centres (ion-radical $\equiv Si\cdot$ or SiO_3^{3-}), whereas multi-

electron centres - aggregates of simple centres, X-centres and colloidal lithium (Li_n). The grey and "black" colour of the irradiated modified and reference Li_4SiO_4 pebbles practically disappears after thermal treatment up to 973 K, most likely due to the transformation and thermally stimulated recombination processes of simple and multi-electron type centres.

After irradiation up to 5 GGy absorbed dose, no major changes in the structure of the modified Li_4SiO_4 pebbles with 10-30 mol% Li_2TiO_3 were observed by p-XRD and FT-IR spectroscopy. However, due to the small decomposition degree (α) of Li_4SiO_4 and Li_2TiO_3, and detection limits of p-XRD and FT-IR spectroscopy, major changes were not expected.

Qualitative analysis of radiation-induced defects and radiolysis products in modified Li_4SiO_4 pebbles with additions of TiO_2.

The formation of hole and electron type RD and RP in the reference Li_4SiO_4 pebbles during irradiation with accelerated electrons take place through three main stages. In the first stage of the radiolysis forms primary stage RD, like, E' centres (SiO_3^{3-}) and HC_2 centres (SiO_4^{3-}), due to dissociation of triplet excitons on oxygen ions (L-centre). In the second and third stage of radiolysis forms secondary RD, like, peroxide radicals ($\equiv$Si-O-O·) etc., and chemically stable RP, like, molecular oxygen (O_2), colloidal lithium (Li_n) and colloidal silicon (Si_n) etc.

Previously it has been determined that after irradiation up to 11 GGy absorbed dose at 550–590 K in dry argon atmosphere, up to 95 % of the accumulated electron type RD and RP in the reference Li_4SiO_4 pebbles are RP (Li_n particles), while the rest are RD (E', F^+ and F^o centres). The E' centres, Li_n particles and F^+ centres may possess paramagnetic properties and thus could be detected and analysed by ESR spectroscopy. The F^+ centres forms broad ESR signal with hyperfine structure (g=2.0030, $\Delta H \approx 20$ mT) while the E' centre forms only one characteristic signal (g=2.001, $\Delta H \approx 1$ mT).

In the ESR spectra of the reference Li_4SiO_4 pebbles with 10 mol% Li_2SiO_3 after irradiation the formation four signals with g-factor from 2.032 to 2.002 were observed. These signals were attributed to the E′ centres (g=2.002±0.003), HC_2 centres (g_1=2.014±0.003 and g_2=2.020±0.003) and peroxide radicals (g=2.032±0.003), which have been investigated and characterized in previous experiments. Presumably the signals of F^+ centre in the ESR spectra are too broad to be analysed. Whereas in the ESR spectra of the modified Li_4SiO_4 pebbles with 10-30 mol% Li_2TiO_3 the formation of two main groups of the first derivative signals were detected. The first group consist of five signals with g-factor from 2.037 to 2.004 while the second group from three signals with g-factor from 1.97 to 1.93.

The signals of the first group (g_1=1.996±0.003, g_2=2.004±0.003, g_3=2.012±0.003, g_4=2.015±0.003 and g_5=2.037±0.003) in the ESR spectra of the modified Li_4SiO_4 pebbles are characteristic to the paramagnetic RD and RP, which form and accumulate in "pure" Li_4SiO_4, Li_2SiO_3, SiO_2 and Li_2TiO_3 ceramic. Therefore, the ESR signal with a g-factor 2.004±0.003 could be attributed to E' centres (SiO_3^{3-}/TiO_3^{3-}), in contrast to the signals with g-factor 2.012±0.003 and 2.015±0.003, which can be assigned to HC_2 centres (SiO_4^{3-}/TiO_3^-). The ESR signal with g-factor 2.037±0.003 could be attributed to peroxide radicals, whereas the broad signal with g-factor 1.996±0.003 could be associated as part of the characteristic Dysonian signals of large Li_n particles.

The second group of signals (g_1=1.97±0.01, g_2=1.95±0.01 and g_3=1.92±0.01) in the ESR spectra of the modified Li_4SiO_4 pebbles are broad, complex and uncharacteristic to the reference pebbles. Therefore it has been assumed that these broad, complex and uncharacteristic signals in the modified pebbles also could be also assigned to the

paramagnetic metallic impurities, for example, Pt^{3+} and Pt^+ ions. Due to that, all of them in the next text were entitled as un-identified RD.

The ESR signals of E' and HC_2 centres, peroxide radicals, broad Li_n particles and un-identified RD in the modified and reference Li_4SiO_4 pebbles practically disappears after thermal treatment up to 973 K. Most likely due to the transformation and thermally stimulated recombination processes of RD and RP. After 973 K in the ESR spectra of the reference pebbles only one, quite narrow and small signal (g=2.001±0.003, ΔH≈0.4 mT) was detected, most likely due to the short annealing time. It has been assumed that this ESR signal could be associated with Li_n particles which have the size <1 μm.

Quantitative analysis of paramagnetic radiation-induced defects and radiolysis products in modified Li_4SiO_4 pebbles with additions of TiO_2.

To compare the radiation stability of the modified Li_4SiO_4 pebbles with reference pebbles, the concentration of E' centres, HC_2 centres, peroxide radicals and Li_n particles were selected as main comparative parameter. These electron and hole type RD and RP were selected, due to the possible interaction with tritium and formation of stable chemical bonds. Whereas, the concentration of the un-identified RD were not further analysed, due to broad, complex and overlapped signals in the ESR spectra.

The Li_2TiO_3 has smaller decomposition degree and radiation chemical yield of RD than Li_2SiO_3, and thus could increase the radiation stability of the modified Li_4SiO_4 pebbles. Obtained results clearly confirm this suggestion and by replacing Li_2SiO_3 with equal molar amount of Li_2TiO_3 phase, the concentration of paramagnetic RD significantly decreases. However, the analysis of RD formation as a function of the content of Li_2TiO_3 in modified Li_4SiO_4 pebbles requires additional experiments. It has been assumed that this effect could be related to several factors, like, microstructure and grain size of modified Li_4SiO_4 pebbles or different content of metallic impurities, like, platinum.

In the reference Li_4SiO_4 pebbles after irradiation mainly E' centres accumulate – up to 75 %, most likely due to the elevated irradiation temperature and high absorbed dose. Whereas concentration of HC_2 centres, peroxide radicals and broad Li_n particles are quite small. The concentration of Li_n particles has to be regarded with suspicion, due to the ESR signal overlap and particle aggregation. Replacing Li_2SiO_3 with equal molar amount of Li_2TiO_3 as secondary phase in the Li_4SiO_4 pebbles the concentration of E' centres rapidly decreases.

The hole and electron type RD and RP in the reference and modified Li_4SiO_4 pebbles are formed in equivalent amounts. The E' and HC_2 centres are the primary stage electron and hole type RD of Li_4SiO_4 and Li_2TiO_3. Peroxide radicals are formed in the second stage of a sample radiolysis. The colloidal Li_n forms at the radiolysis of the Li_4SiO_4 and Li_2TiO_3 as a result of coagulation of the electron type RD.

Obtained results indicate that by replacing Li_2SiO_3 with equal molar amount of Li_2TiO_3 phase in the pebbles, the concentration of paramagnetic RD and RP decreases slightly. Therefore it can be concluded that the modified Li_4SiO_4 pebbles with 10-30 mol% Li_2TiO_3 have slightly higher radiation stability compared with the reference pebbles. Increasing absorbed dose from 1 to 5 GGy, the total concentration of RD and RP in the reference and modified Li_4SiO_4 pebbles slightly decreases. The rapid decrease of RD and RP concentration in the modified and reference pebbles after irradiation up to 3.5 GGy was attributed to the thermally stimulated recombination, due to the elevated temperature in last irradiation cycle (T≈660 K).

The high-temperature radiolysis of the modified Li_4SiO_4 pebbles with different content of TiO_2 were investigated and described for the first time. Obtained results also confirm suggestion that the modified Li_4SiO_4 pebbles could have higher radiation stability compared with the reference pebbles. Therefore the modified pebbles have the potential to combine the advantages of Li_4SiO_4 and Li_2TiO_3 as a tritium breeding ceramic. However, all above mentioned results also clearly confirms necessity to further study the radiation-induced chemical processes, microstructural changes and phase transitions in the modified Li_4SiO_4 pebbles, which will occur under the exploitation conditions of the HCPB TBM.

5. STAFF MOBILITY ACTIONS

5.1. STAFF MOBILITY VISITS

J.Mastrikovs	Vācija, KIT, Karlsruhe, 01.06-16.06.2013
J.Žukovskis	Vācija, KIT, Karlsruhe, 02.06-16.06.2013
J.Mastrikovs	Vācija, KIT, Karlsruhe, 12.08-31.08.2013
O. Dumbrajs	Vācija, KIT, Karlsruhe, 07.09-30.09.2013
J. Zhukovskis	Vācija, KIT, Karlsruhe, 07.09-30.09.2013
O. Dumbrajs	Vācija, KIT, Karlsruhe, 01.10-31.10.2013
A.Gopejenko	Vācija, KIT, Karlsruhe, 18.11-18.12.2013
G.Ķizāne	Lielbritānija, Kalema, 10.06-14.06.2013

6. OTHER ACTIVITIES

6.1. Conferences, Workshops and Meetings

Results of fusion research were presented at the conferences:

1. General Technical Meeting of the JET Task Force–Fusion Technology (TF-FT) work, Semi-annual monitoring meeting of "JW13-FT-1.21" and "JW13-FT-1.23", 11–14 June, 2013, the JET, Culham Science Centre, Abingdon, UK. Oral presentation
2. Semi-annual monitoring meeting - JET Fusion Technology on the tasks JW13-FT-1.21 and JW13-FT-1.23, 10-13 December, 2013.

7. PUBLICATIONS 2013

7.1. FUSION PHYSICS AND PLASMA ENGINEERING

7.1.1. Publications in scientific journals
1. O. Dumbrajs and G.S. Nusinovich *"Effect of electron beam misalignments on the gyrotron efficiency"* Phys. Plasmas **20**, 073105 (2013).

7.1.2. Conference articles
1. 40th European Physical Society conference on plasma physics, July 1-5, 2013, Espoo, Finland.
2. 38th International Conference on Infrared, Millimeter and Terahertz Waves, September 1-6, 2013, Mainz, Germany.
3. *29th ISSP Conference (Riga, Latvia, February, 2013).* A. Gopejenko, Yu.F. Zhukovskii, P.V. Vladimirov, E.A. Kotomin, J.Mastrikov, and A. Möslang, "*Ab initio* calculations of Y and vacancies interactions in fcc Fe lattice". Abstracts: p. 61.
4. 11th *International Conference "Information Technologies and Management", IT&M'2013 (Riga, Latvia, April, 2013).*A. Gopejenko, Yu.F. Zhukovskii, P.V. Vladimirov, E.A. Kotomin, Yu.A. Mastrikov, and A. Möslang, "First principles modeling of interactions between Y, O and vacancies in *fcc*-Fe lattice". Abstracts: p. 112-114.
5. *9th International Conference "Functional Materials and Nanotechnologies" FM&NT-2013 (Tartu, Estonia, April, 2013).*Yu.F. Zhukovskii, A. Gopejenko, Yu.A. Mastrikov, E.A. Kotomin, P.V. Vladimirov, and A. Möslang, "Modeling of Y-O precipitation in *bcc*-Fe and *fcc*-Fe lattices." – Abstract: OR-35.
6. *Annual Monitory Meeting of European Fusion Development Agreement, EFDA - 2013 (Bucharest, Romania, June, 2013).*Yu.A. Mastrikov, P.V. Vladimirov, V.A. Borodin, Yu.F. Zhukovskii, E.A. Kotomin, and A. Möslang, "*Ab initio* modeling of nY/nV_{Fe} complexes diffusion in the α-Fe lattice."
7. EFDA MAT – IREMEV Monitoring Meeting, (Garching, Germany, February 2014) Yu.A. Mastrikov, P.V. Vladimirov, V.A. Borodin, Yu.F. Zhukovskii, E.A. Kotomin, and A. Möslang "*Ab initio* modeling of the 2Y/3V cluster migration in the *bcc* Fe lattice."
8. *30th ISSP Conference (Riga, Latvia, February, 2014).* A. Gopejenko, Yu.F. Zhukovskii, P.V. Vladimirov, E.A. Kotomin, Yu.A Mastrikov, V.A. Borodin and A. Möslang, "First principles calculations of the energy barriers for different trajectories of Y atom migration inside *fcc*-Fe lattice". Abstracts: p. 36.
9. *12th International Conference "Information Technologies and Management", IT&M'2014 (Riga, Latvia, April, 2014).* A. Gopejenko, Yu.F. Zhukovskii, P.V. Vladimirov, E.A. Kotomin, Yu.A. Mastrikov, V.A. Borodin and A. Möslang, "*Ab initio* calculations of interactions between Y, O impurity atoms and Fe vacancies for ODS steel implementation in fusion reactors". Abstracts: p. 21-22.

7.2. Fusion Technology
7.2.1. Publications in scientific journals

1. C. Stan-Sion, M. Enachescu, A. Petre, M. Duma, D.G. Ghita, G. Kizane, L. Baumane, J. Gabrusenoks, M. Halitovs, L. Avotina, A. Zarins, J. Likonen, S. Koivuranta, M. Kiisk and JET EFDA contributors. Intercomparison of AMS and

FC Measurements of Tritium in Laser Cleaned Tile. Accepted "*Fusion Engineering and Design*", 2013.

2. A. Vītiņš, G. Ķizāne, A. Matīss, E. Pajuste, V. Zubkovs, Tritium release behavior of beryllium pebbles after neutron irradiation between 523 and 823 K, J. Nucl. Mater. (2013), in press, 4 p., http://dx.doi.org/10.1016/j.jnucmat.2013.03.037

3. A. Zarins, G. Kizane, A. Supe, R. Knitter, M. H.H. Kolb, J. Tiliks Jr., L. Baumane. Influence of chemisorption products of carbon dioxide and water vapour on radiolysis of tritium breeding ceramic. Fusion Engineering and Design (2014) *in-press,* http://dx.doi.org/10.1016/j.fusengdes.2014.01.005

4. A.Marcu, L. Avotina, A. Marin, C. P. Lungu, C. E. A. Grigorescu, N. Demitri, D. Ursescu, C. Porosnicu, P. Osiceanu, G. Kizane and C. Grigoriu. Laser irradiation of Carbon-Tungsten materials, submitted "*Journal of Physics D: Applied Physics*", 2013.

5. C. Stan-Sion, M. Enachescu, A. Petre, M. Duma, D.G. Ghita, G. Kizane, L. Baumane, J. Gabrusenoks, M. Halitovs, L. Avotina, A. Zarins, J. Likonen, S. Koivuranta, M. Kiisk and JET EFDA contributors. Intercomparison of AMS and FC Measurements of Tritium in Laser Cleaned Tile. Accepted "*Fusion Engineering and Design*", 2013.

6. A. Vītiņš, G. Ķizāne, A. Matīss, E. Pajuste, V. Zubkovs, Tritium release behavior of beryllium pebbles after neutron irradiation between 523 and 823 K, J. Nucl. Mater. (2013), in press, 4 p., http://dx.doi.org/10.1016/j.jnucmat.2013.03.037

7. A. Zarins, G. Kizane, A. Supe, R. Knitter, M. H.H. Kolb, J. Tiliks Jr., L. Baumane. Influence of chemisorption products of carbon dioxide and water vapour on radiolysis of tritium breeding ceramic. Fusion Engineering and Design (2014) *in-press,* http://dx.doi.org/10.1016/j.fusengdes.2014.01.005

8. A.Marcu, L. Avotina, A. Marin, C. P. Lungu, C. E. A. Grigorescu, N. Demitri, D. Ursescu, C. Porosnicu, P. Osiceanu, G. Kizane and C. Grigoriu. Laser irradiation of Carbon-Tungsten materials, submitted "*Journal of Physics D: Applied Physics*", 2013.

8.2.2. Conference articles

1. L. Avotina, G. Kizane, J. Kalnacs, L. Baumane, L. Ansone. Thermal analysis of plasma unaffected JET divertor powders in inert and air atmosphere. *International conference "Functional Materials and Nanotechnologies 2013"* (FM&NT 2013), Tartu, Estonia, 21-24 April 2013, The Book of Abstracts FM&NT-2013, p.219

2. L. Avotina, G. Kizane, A. Matiko, J. Kalnacs, A. Petjukevics**.** Analysis of Fullerene C_{60} Possible Formed in the Divertor Area of a Tokamak Like Devices. 3rd PhD Event in Fusion Science and Engineering, York, UK, June 22-16, 2013, Book of abstracts 3rd PhD even tin Fusion Science and Engineering, p.12.

3. M. Halitovs, L. Avotina, G. Kizane, J. Lapins, L. Baumane, J. Kalnacs. Comparison of physicochemical properties of fullerene C_{60} in crystal and powder form. *2nd Central and Eastern European Conference on Thermal Analysis and Calorimetry* (CEEC-TAC2), Vilnius, Lithuania, 27.-30. August, 2013, CEEC-TAC2 book of abstracts, p.187

4. A.Zarins, G. Kizane, R. Knitter, A. Supe. Influence of chemisorption products of carbon dioxide on radiolysis of tritium breeding ceramic. 11th International

Symposium on Fusion Nuclear Technology (ISFNT-11), September 16-20, 2013, Barcelona, Spain. Abstract book, Barcelona, Spain, P3-036, p. 436.

5. <u>A.Zarins</u>, G. Kizane, A. Supe, R. Knitter, M. Kolb, L. Baumane, O. Valtenbergs. Influence of Li_2TiO_3 on radiolysis of Li_4SiO_4 pebbles. 17th IEA International Workshop on the Ceramic Breeder Blankets: Ceramic Breeder Blanket Interactions (CBBI-17), September 12-14, 2013, Barcelona, Spain. *Abstracts,* 2013, p. 9.

6. <u>A.Zarins</u>, G. Kizane, R. Knitter, M. Kolb, A. Supe, J. Kalnacs, O. Valtenbergs. Characterization of Li_4SiO_4 pebbles with TiO_2 additions, using methods of thermal analysis. 2nd International Central and Eastern European Conference for Thermal Analysis and Calorimetry, August 27-30, 2013, Vilnius, Lithuania. Book of abstracts, Vilnius, Lithuania, PS.2.48, p.302.

7. <u>A.Zarins</u>, G. Kizane, A. Supe, R. Knitter, M. Kolb, L. Baumane, O. Valtenbergs. Radiation stability of differently synthesized and pre-treated tritium breeding ceramic. 3rd PhD Event in Fusion Science and Engineering, June 22-26, 2013, York, United Kingdom. *Book of abstracts,* 2013, p. 71.

8. <u>A.Zarins</u>, G. Kizane, A. Supe, R. Knitter, M. Kolb, O. Leys. Influence of Li_2TiO_3 on chemical reactivity of Li_4SiO_4 pebbles. International conference "Functional Materials and Nanotechnologies 2013" (FM&NT 2013), April 21-24, 2013, Tartu, Estonia. *Book of abstracts,* 2013, PO-154.